ELSEVIER

Chemical Geology 219 (2005) 5–35

CHEMICAL GEOLOGY
INCLUDING
ISOTOPE GEOSCIENCE

www.elsevier.com/locate/chemgeo

Petrogenesis of the Linxi granitoids, northern Inner Mongolia of China: Constraints on basaltic underplating

Wei Liu[a,*], Wolfgang Siebel[b], Xin-jun Li[a], Xiao-fei Pan[a]

[a]*State Key Laboratory of Lithosphere Tectonic Evolution, Institute of Geology and Geophysics, Chinese Academy of Sciences, Beijing 100029, China*
[b]*Institut für Mineralogie, Petrologie und Geochemie, Universität Tübingen, 72074 Tübingen, Germany*

Received 30 March 2004; accepted 17 January 2005

Abstract

Five representative granitoid plutons in the Linxi area, northern Inner Mongolia of China, divided into two suites, are mainly granodiorite and syenogranite and correspond to I- and A-type granites, respectively. Zircon U–Pb dating yields an age of ~ 230 Ma, but most ages range from 149 Ma to 111 Ma for intrusion of the five plutons. Suite 1 granitoids show lower SiO_2 (66.1–72.51%) and K_2O, higher Al_2O_3, CaO, MgO, FeO, and TiO_2, higher Sr, Ba, and Eu, and lower Sm + Gd, Nb, Y, and Yb than Suite 2 granitoids (71.73–78.14% SiO_2). Modeling of major and trace elements shows that fractional crystallization of hornblende and lesser amounts of feldspars for Suite 1 and plagioclase and alkali feldspar for Suite 2, with overprint of magmatic hydrothermal fluids, can explain the geochemical variations. The Linxi granitoids have initial $\varepsilon_{Nd}(t)$ values varying between +5.60 and −2.89, and initial $(^{87}Sr/^{86}Sr)_t$ ratios ranging from 0.701764 to 0.707654. Geochronology of inherited zircons, coupled with the Nd, Sr isotopic comparison between granitoids, Late Jurassic basalts, and Proterozoic gneisses, indicates that the Linxi granitoids derive from a mixed source of dominantly underplated material or mafic magma with various amounts of the Proterozoic gneiss. Basaltic underplating provides both material and heat to produce the Late Jurassic to Early Cretaceous granitoids. Variation of $\varepsilon_{Nd}(t)$ and $(^{87}Sr/^{86}Sr)_t$ with age suggests involvement in the melting of increasingly greater amounts of the old lower-crustal rock. Our refined equation yields less scattered Nd isotope depleted mantle model ages. The least-fractionated granitoids from each suite have low Ca/Sr, Rb/Sr, Rb/Ba, and K/Ba ratios and, hence, represent parental magmas. Suite 1 parent magma is produced by dehydration melting or derives principally from the fluid-metasomatized mantle. Melting of the underplated tholeiites and their differentiated products generates Suite 2 parent magma.

Keywords: Basaltic underplating; Continental crust growth; Granitoid petrogenesis; Northern Inner Mongolia

1. Introduction

Phanerozoic granitoids in the western segment of the Central Asian Orogenic Belt are characterized by

* Corresponding author. Tel.: +86 1 010 62007557.
E-mail address: liuw@mail.igcas.ac.cn (W. Liu).

0009-2541/$ - see front matter © 2005 Elsevier B.V. All rights reserved.
doi:10.1016/j.chemgeo.2005.01.013

generally positive $\varepsilon_{Nd}(t)$ values, young T_{DM} ages, and low initial $(^{87}Sr/^{86}Sr)_t$ ratios (e.g., Kwon et al., 1989; Zanvilevich et al., 1995; Kovalenko et al., 1996; Han et al., 1997). These characteristics reflect addition of juvenile crust (e.g., Sengör et al., 1993). The eastern segment of the Central Asian Orogenic Belt includes the eastern and southern central Mongolia, northern Inner Mongolia of China, and northeastern China. In this region, extensive volcanism occurred in the Late Jurassic and continued into the Early Cretaceous time (Graham et al., 2001; Yarmolyuk and Kovalenko, 2001). These volcanics consist mainly of mafic to intermediate and alkaline rocks, and show low $(^{87}Sr/^{86}Sr)_t$ and high $\varepsilon_{Nd}(t)$ values (Chen and Chen, 1997; Yarmolyuk and Kovalenko, 2001). In this region, the widespread late Mesozoic granitoids, dominantly alkaline and peralkaline, show low $(^{87}Sr/^{86}Sr)_t$ and positive $\varepsilon_{Nd}(t)$ values (Wu et al., 2000; Yarmolyuk and Kovalenko, 2001).

The characteristics of low $(^{87}Sr/^{86}Sr)_t$ and high $\varepsilon_{Nd}(t)$ values are shared by Phanerozoic granitoids in areas such as the New England and the Lachlan Belts, southeastern Australia (Hensel et al., 1985; Eberz et al., 1990; Bryant et al., 1997; Keay et al., 1997; King et al., 1997), the Cordillera of North America (Samson et al., 1989; Coleman et al., 1992; Cui and Russell, 1995; Friedman et al., 1995; Pickett and Saleeby, 1999), Newfoudland Appalachians, Canada (Whalen et al., 1996), and the Africa (Kinnaird and Bowden, 1987; Bowden et al., 1990). The Proterozoic A-type granites in Labrador, Canada (Kerr and Fryer, 1993) and rapakivi-type anorogenic granites in the southwestern USA (Frost et al., 1999), and the fayalite or high-silica rhyolites in the Yellowstone–Snake River Plain province (Hildreth et al., 1991) and the Basin and Range province (Bacon et al., 1981; Novak and Mahood, 1986), USA, show similar characteristics. Re-melting of newly underplated tholeiites and their differentiated products generated these reduced rapakivi-type granites and their eruptive equivalents, high-K fayalite rhyolites (Frost and Frost, 1997). However, this hypothesis is constrained merely by low oxygen fugacity and pronounced iron enrichment in these rocks, whereas direct evidence for the underplating is lacking. Specifically, petrogenesis of these granitoids that has important implications for the continental crust growth under extensional regime in general and in the eastern segment of the Central Asian Orogenic Belt in particular is poorly understood. The present study was conducted with the aim to illuminate the above problems.

2. Regional geological setting

As shown in Fig. 1, the eastern segment of the Central Asian Orogenic Belt is divided into the Altaid and the Xingmeng (Sengör and Natal'in, 1996). The Linxi area lies in the Xingmeng belt. This region has undergone the evolution of the Paleo-Asian Ocean in the Paleozoic through Triassic times, and collision-related compression followed by extension in Mesozoic times (Meng, 2003). The Xingmeng and the Altaid were amalgamated along the Ondor Sum–Xilinhot–Linxi suture by the end of the Paleozoic time (e.g., Yin and Nie, 1996; Lamb and Badarch, 1997).

Proterozoic metamorphic complex is the most ancient rock unit within the northern Inner Mongolia. The nearest outcrop of this unit occurs about 30 km to the southeast of the Linxi town (Fig. 1), and consists of amphibole plagioclase gneiss, biotite granitic gneiss, and mica shists. Ordovician to Permian strata are dominantly detrital rocks with minor carbonate rocks. However, the Lower Permian strata are dominantly mafic to intermediate lavas and lava breccia.

During the Early Jurassic, crust around the Linxi area was uplifted as evidenced by the absence of the Early Jurassic sediments. During the late Middle through early Late Jurassic time, collision of the North China–Mongolia block with the Siberia plate along the Mongol–Okhotsk suture to the north resulted in thrust faulting in the northeast–southwest direction and inversion structures in the Mesozoic basins (Zorin et al., 1995; Kravchinsky et al., 2002). Extensional tectonism that includes rifted basins, alkaline and peralkaline granitoid plutonism, and metamorphic core complexes prevailed in the northern Inner Mongolia in the late Late Jurassic through Early Cretaceous time (Zheng et al., 1991; Webb et al., 1999; Davis et al., 2002). Rifted basins were initiated by voluminous volcanic eruption, and culminated in the Early Cretaceous (Meng, 2003). The volcanics consist mainly of basalt, alkaline basalt, andesite, trachyandesite, trachyte, and subordinate rhyolite, with a petrogenetic succession from mafic to felsic.

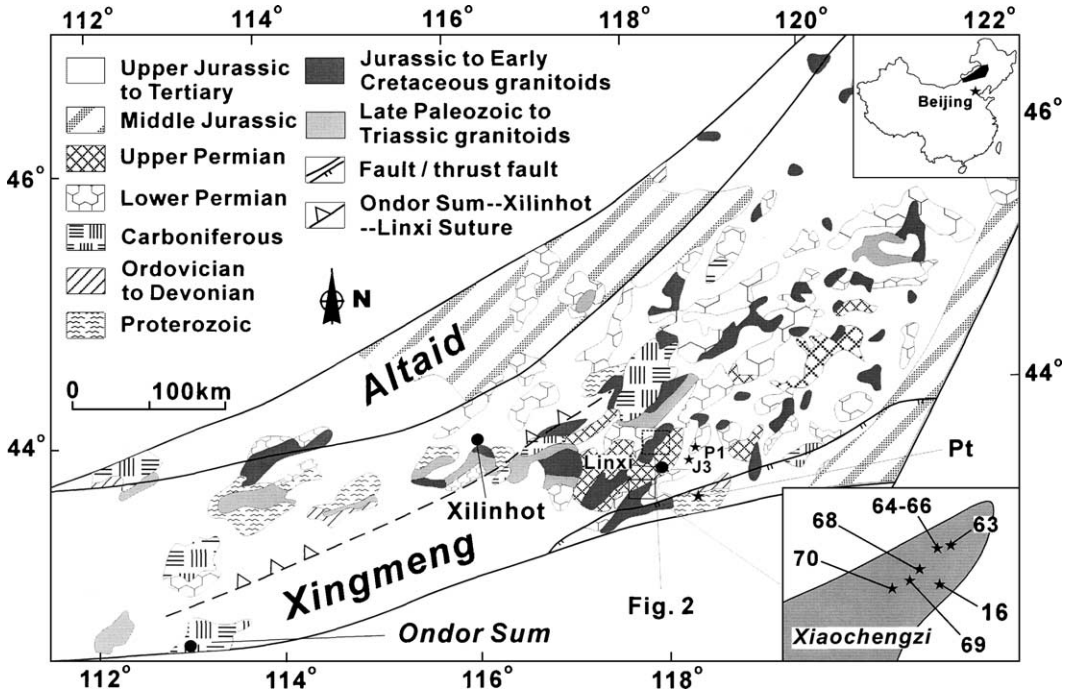

Fig. 1. Geological sketch map of the northern Inner Mongolia. The upper inset shows the location of the northern Inner Mongolia (the shaded area) within China. The lower inset shows sampling locations (stars) in the Xiaochengzi pluton, with the last two numbers from the sample name. Stars labeled with P1 and J3 show sampling locations from the Early Permian and the Late Jurassic eruptive rocks. Star labeled with Pt shows the sampling location from the Proterozoic gneisses.

Granitoid plutonism is concurrent with the volcanism, but became more vigorous in the Early Cretaceous time following the peak of volcanism. These extensional basins underwent little or no post-rift thermal subsidence, which, integrated with intense granitoid plutonism, implies an elevated geothermal gradient to the Early Cretaceous time (Buck, 1991).

3. Petrography

We selected five granitoid plutons from the Linxi area for this study. These plutons are the Maanzi, the Yelaigai, the Longtoushan 1, the Longtoushan 2 (Fig. 2), and the Xiaochengzi (the lower inset of Fig. 1). According to petrographic characteristics (Table 1), the Xiaochengzi and the Longtoushan 1 were classified as Suite 1, whereas the Maanzi, the Yelaigai, and the Longtoushan 2 are Suite 2. Suite 1 is granodiorite with subordinate monzogranite. Plagioclase that predominates over perthite is mainly andesine with oscillatory zoning. Besides biotite, hornblende and skeletal pyroxene that is often included within biotite also occur. Accessory minerals include ilmenite, apatite, zircon, sphene, and trace allanite. Suite 2 is syenogranite with subordinate monzogranite and minor granodiorite porphyry. Perthite predominates over plagioclase that is mainly oligoclase. Quartz has a higher percentage (23–32% by volume) than that of Suite 1 (21–26%). Besides biotite, minor skeletal pyroxene (< 1%) was included within biotite. However, except within the Longtoushan 2, hornblende was not observed. Accessory minerals include ilmenite, apatite, zircon, fluorite, xenotime, and trace allanite.

4. Experimental procedures

As shown in Fig. 2 and the lower inset of Fig. 1, 34 granite samples were collected from the five plutons. Samples of basalt (S1718, S1805, S1815), alkaline

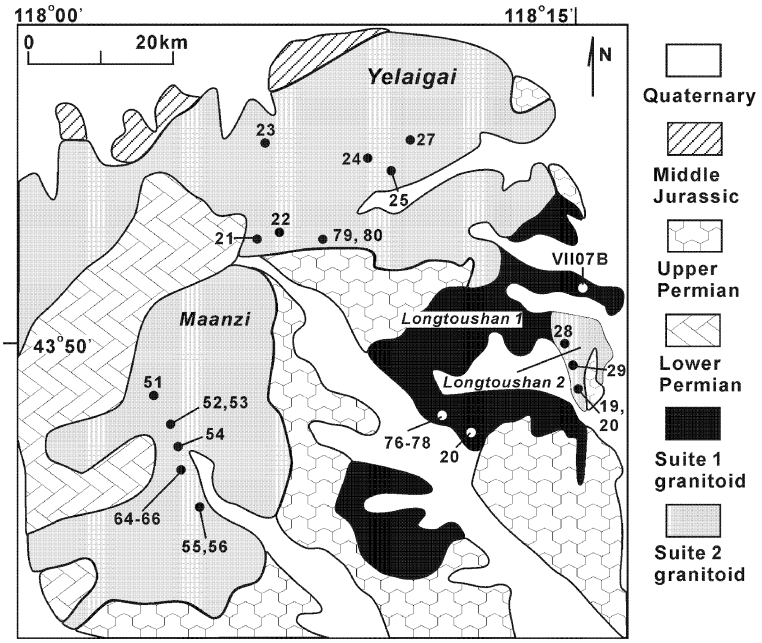

Fig. 2. Sketch map showing sampling locations from the Yelaigai, the Maanzi, the Longtoushan 1, and the Longtoushan 2 plutons. The dot and the number represent the sampling location and the last two numbers from the sample name.

basalt (S2001), and andesitic basalt (S2406, S2501) were collected from the Late Jurassic eruptive rocks (Fig. 1). Samples of amphibole plagioclase gneiss (DB-101, FL62404, FL62406) and biotite granitic gneiss (DB-102, FL62405) were collected from the Proterozoic metamorphic complex (Fig. 1).

4.1. Major element and trace element analyses

Major and trace element compositions were analyzed in the State Key Laboratory of Lithosphere Tectonic Evolution, Institute of Geology and Geophysics, and the Guangzhou Institute of Geochemistry, Chinese Academy of Sciences (CAS), respectively. Rock samples weighing more than 1 kg were crushed and milled to 200 mesh and then thoroughly mixed. Major elements were analyzed on discs fused using 5:1 dilution with anhydrous lithium tetraborate. The analyses were performed on a Sequential X-Ray Fluorescence Spectrometer (XRF). Precisions are of the order of 0.1 wt.% or better for major elements. For the measurement of FeO, 0.1 to 0.2 g of powdered samples (~100 mesh) were decomposed with H_2SO_4 and HF solution, and then titrated using a standardized $K_2Cr_2O_7$ solution.

For the analysis of trace element abundances, about 40 mg was taken from each powdered sample and decomposed with HF–$HClO_4$ in Teflon bomb at 200 °C for more than 1 week. After addition of In as an internal standard, sample solutions were diluted with 1% HNO_3. The analysis was performed on a High Resolution Inductively Coupled Plasma Mass Spectrometer (Finnigan-MAT). The geostandard W-2 was used as standard sample that was checked after every five samples. Trace element abundances analyzed on the W-2, and its recommended values (Govindaraju, 1994) are listed in Table 2. The accuracy is better than 10% for all the trace elements except Pb and Zn by our analysis. Moreover, as shown in Tables 2, 4 and 5, the accuracies for Rb, Sr, Sm, and Nd abundances by the ICP-MS analysis are better than 10% compared with the isotope dilution analysis on the granite samples.

4.2. Isotope dilution U–Pb dating on zircon

Samples LW97077 (Longtoushan 1), LW97066 (Maanzi), WL60423 (Yelaigai), WL60428 (Longtoushan 2), and WL53063 (Xiaochengzi) were selected for the zircon U–Pb dating. Zircons were

Table 1
Petrography of the five representative granitoid plutons in the Linxi area[a]

Suite	Pluton	Rock type	Color	Texture	Plagioclase (volume content)	Perthite	Quartz	Biotite	Hornblende	Pyroxene	Accessory minerals
1	Xiaochengzi	Biotite granodiorite and monzogranite	Greyish white	Medium to coarse-grained	Ads and Olg (40–52%) with oscillatory zoning	17–27%	24–26%	2–8%	< 1–3%	Skeletal in Bt (<1%)	Zc, Ap, Ilm, Sph
	Longtoushan 1	Hornblende biotite granodiorite and monzogranite	*idem*	Medium to fine-grained	Ads and Olg with oscillatory zoning, 25–63%, mostly 40–50%	12–44%, mostly 13–28%	21–26%	3–7%	2–5%	Skeletal in Bt, < 1–2%	Ilm, Ap, Zc, Sph, Aln
2	Longtoushan 2	Hornblende biotite syenogranite and granodiorite porphyry	Greyish	Porphyritic, 15–50%	Olg and Ads, 30–50%	25–40%	23–32%	< 1–3%	1–3%		Ilm, Ap, Zc, Aln
	Maanzi	Biotite syenogranite and monzogranite	Yellowish, pink, greyish white	Medium to fine-grained	Olg and Ads, 18–30%	37–50%	25–30%	3–8%		< 1%	Ilm, Ap, Zc, Flr, Xt, Aln
	Yelaigai	Biotite syenogranite and monzogranite	*idem*	Medium to coarse-grained	Olg and Ads, 21–40%	32–46%	25–32%	2–7%		< 1%	Ilm, Ap, Zc, Flr, Xt, Aln

[a] Olg: oligoclase; Ads: andesine; Bt: biotite; Ilm: ilmenite; Zc: zircon; Flr: fluorite; Xt: xenotime; Ap: apatite; Sph: sphene; Aln: allanite.

separated from the whole-rock sample weighing up to 5 kg, employing magnetic separator and heavy liquids. Zircons were chosen and divided into fractions according to color, grain size, crystal form, and integrity of crystal form. Representative zircons for each population were mounted in epoxy and then polished to expose the internal texture. We inspected zircons using the binocular microscope, transmitted and reflected light microscope, and cathodoluminescence technique to look for magmatic zonation, xenocrystic cores, and recrystallized areas. Typical internal textures of zircon are shown in Fig. 3. Petrographic features for each fraction of the zircon separates are briefly described in Table 3.

We carried out the U–Pb isotope dating on zircon in the Institut für Mineralogie, Petrologie und Geochemie, Universität Tübingen, Germany. Each zircon fraction was abraded according to the method of Krogh (1982) and then washed in hot 6 N HCl and hot 7 N HNO_3, respectively. Zircon fractions were spiked with a ^{205}Pb–^{233}U tracer solution and decomposed at 200 °C for 6 days. Zircon fractions were transferred into polytetrafluorethylene vessels that fit a Teflon-lined Parr bomb (Parrish, 1987). Then, 22 N HF was supplied in the bottom of the Teflon bomb, enabling vapor digestion. After decomposition of the zircons, the HF in the Teflon bomb was replaced with 6 N HCl, and the bomb was heated for 1 day to convert fluoride salts to more soluble chloride salts. Separation and purification of U and Pb were performed on Teflon columns with a 20-μl bed of AG1-X8 (100–200 mesh) anion exchange resin (Poller et al., 1997; Chen et al., 2000). The total procedural blanks for Pb and U were approximately 12 and 5 pg, respectively. The isotopic composition of the Pb blank contribution was $^{206}Pb/^{204}Pb = 18.5$ and $^{207}Pb/^{204}Pb = 15.5$.

Measurement of U and Pb isotope ratios was performed on a Finnigan MAT 262 mass spectrometer operated in static collection mode. Pb was loaded with a mixture of Si gel and H_3PO_4 onto a single-Re filament and measured at 1300 °C. U was loaded with 1 N HNO_3 onto a Re filament and measured in a double-filament configuration. The lead standard NBS 981 was measured to determine the thermal fractionation of Pb isotopes, and the isotopic ratios were corrected for 0.11% fractionation per atomic mass unit. Data regression was performed with ISOPLOT (Ludwig, 1994).

Table 2
Major element oxide contents (wt.%) and trace element abundances (ppm) of the Linxi granitoids[a]

Pluton/suite	Sample no.	SiO_2	TiO_2	Al_2O_3	MnO	MgO	FeO	Fe_2O_3	CaO	Na_2O	K_2O	P_2O_5
Maanzi Suite 2	WL852651	75.27	0.05	12.48	0.02	0.02	0.85	0.13	0.31	4.07	4.45	0.01
	WL852652	74.22	0.18	12.81	0.03	0.18	1.40	0.28	0.74	3.70	4.92	0.04
	WL852653	76.81	0.08	12.06	0.01	0.05	0.75	0.35	0.40	3.60	4.56	0.01
	WL852654	75.33	0.12	12.86	0.03	0.11	0.90	0.18	0.71	3.80	4.65	0.03
	WL852655	74.68	0.17	12.51	0.03	0.17	1.05	0.46	0.66	3.61	4.76	0.04
	WL852656	78.14	0.07	11.37	0.02	0.05	0.60	0.34	0.40	3.33	4.53	0.01
	LW97064	75.40	0.18	12.18	0.04	0.18	1.35	0.27	0.66	3.58	4.55	0.04
	LW97064-1	77.23	0.09	12.00	0.02	0.06	1.00	0.06	0.42	3.49	4.76	0.01
	LW97065	76.90	0.13	11.91	0.03	0.11	1.03	0.27	0.54	3.45	4.52	0.03
	LW97066	75.77	0.12	12.26	0.03	0.10	0.65	0.49	0.57	3.61	4.68	0.02
Yelaigai Suite 2	WL60421	76.19	0.09	12.09	0.02	0.07	0.48	0.71	0.56	3.56	4.62	0.01
	WL60422	74.05	0.14	13.28	0.03	0.11	0.90	0.65	0.65	3.88	5.03	0.02
	WL60423	73.30	0.13	13.33	0.02	0.15	0.75	0.61	0.86	3.88	5.02	0.03
	WL60424	74.51	0.18	13.29	0.04	0.22	0.85	0.79	0.91	3.78	4.71	0.04
	WL60425	71.73	0.30	13.96	0.05	0.40	1.10	0.98	1.36	3.98	4.70	0.08
	LW97079	76.20	0.11	11.93	0.02	0.08	1.45	0.07	0.57	3.29	4.81	0.01
	LW97080	76.05	0.09	12.55	0.02	0.08	0.80	0.44	0.60	3.65	4.85	0.01
Longtoushan 1 Suite 1	WL60420	70.41	0.38	14.60	0.04	0.89	1.95	0.24	2.17	4.00	3.66	0.10
	LW97076	70.56	0.34	14.58	0.04	0.82	1.50	0.46	1.99	3.91	3.95	0.09
	LW97077	70.02	0.36	14.72	0.04	0.85	1.40	0.75	2.09	4.03	3.65	0.10
	LW97078	70.79	0.37	14.62	0.04	0.88	1.50	0.69	2.03	3.93	3.88	0.10
	VII07B	66.10	0.54	14.16	0.07	1.47	1.45	2.68	3.09	3.61	3.64	0.16
Longtoushan 2 Suite 2	WL60428	75.33	0.18	12.47	0.04	0.18	1.25	0.38	0.76	3.74	4.39	0.04
	WL60429	74.72	0.13	12.63	0.05	0.11	0.70	0.85	0.50	4.06	4.44	0.02
	LW97019	74.50	0.13	12.70	0.07	0.13	0.45	1.04	0.59	4.16	4.47	0.02
	LW97020	75.67	0.12	12.78	0.06	0.16	0.50	0.94	0.55	4.18	4.47	0.02
Xiaochengzi Suite 1	WL53063	70.74	0.29	14.08	0.05	0.47	1.45	0.44	1.57	3.86	4.43	0.06
	WL53064	71.90	0.26	14.43	0.04	0.44	1.25	0.50	1.61	3.85	4.54	0.05
	WL53065	71.65	0.27	14.10	0.04	0.45	0.90	0.90	1.52	3.78	4.65	0.06
	WL53066	71.51	0.28	14.04	0.04	0.46	1.40	0.44	1.53	3.72	4.58	0.06
	WL53068	71.60	0.27	14.14	0.04	0.44	1.35	0.44	1.57	3.81	4.58	0.06
	WL53069	71.31	0.29	13.88	0.04	0.48	1.40	0.43	1.57	3.78	4.45	0.06
	WL53070	72.51	0.26	13.98	0.04	0.43	1.08	0.69	1.54	3.73	4.44	0.06
	LW97016	72.19	0.24	13.74	0.04	0.40	0.82	0.86	1.45	3.70	4.57	0.05
This study	W-2											
Recommended[b]	W-2											

[a] A/NKC: $Al_2O_3/(Na_2O+K_2O+CaO)$ (molar); A/NK: $Al_2O_3/(Na_2O+K_2O)$ (molar).
[b] Govindaraju (1994).

4.3. Rb–Sr and Sm–Nd isotope analyses

Rb–Sr and Sm–Nd isotope compositions were analyzed in the State Key Laboratory of Lithosphere Tectonic Evolution, Institute of Geology and Geophysics, CAS. About 50 mg of powdered sample mixed with suitable amounts of Rb–Sr and Sm–Nd spikes was decomposed in Teflon bomb with HF and $HClO_4$ at ~200 °C for about 1 week. After decomposition, samples were transferred to HCl solution. Rb, Sr, and rare earth elements were eluted from the Dowex AG50W × 12 cation exchange resin with 5.0 N HCl. Then, Sm and Nd were eluted from HDEHP (2-ethylhexyl), P204 resin with 0.1 N HCl. Isotope ratios were measured with a Finnigan-MAT262 mass spectrometer operated in static multi-collection mode as metal ions. Rb–Sr and Sm–Nd abundances were determined through isotope dilution. Blanks per analysis ranged from 50 to 100×10^{-11} g for Rb, and were around 50×10^{-11} g for Sr, around 7×10^{-11} g for Sm, and 8×10^{-11} g for Nd. $^{87}Sr/^{86}Sr$ ratios were normalized to $^{86}Sr/^{88}Sr=0.1194$, with uncertainties indicated as $2\sigma_m$. $^{143}Nd/^{144}Nd$ ratios were normalized to $^{146}Nd/^{144}Nd=0.7219$, and uncer-

LOI	Total	A/NKC	A/NK	P	Ti	V	Cr	Mn	Co	Zn	Ga	Rb	Sr
0.58	98.23	1.03	1.08	100.8	383	7.00	104.7	179.7	0.144	29.74	33.09	576.8	5.74
0.73	99.23	1.00	1.12	273.5	1242.2	13.31	206.3	305.6	0.909	11.53	24.87	318.9	58.07
0.74	99.41	1.04	1.11	113.4	541.2	7.37	216.8	99	0.253	5.44	23.85	406.4	8.75
0.62	99.34	1.02	1.14	168.5	816.3	12.14	176.9	216.8	0.433	8.65	21.95	290.4	57.82
0.57	98.70	1.02	1.13	244.2	1031.3	8.87	147	262.5	0.811	15.45	20.57	266.2	50.40
0.61	99.47	1.02	1.10	163.9	629.5	5.82	228.2	129.6	0.064	6.49	20.75	320.1	19.71
0.58	99.00	1.01	1.13	226.6	1238.9	8.66	120.4	348.9	0.573	20.63	22.63	267.8	39.39
0.41	99.55	1.03	1.10	85.8	608.3	3.00	163.4	188.9	0.604	30.81	21.63	246.5	15.91
0.62	99.54	1.03	1.13	124	949.8	7.48	212.1	232.4	0.826	20.42	20.83	222.6	34.87
0.52	98.81	1.02	1.11	137.1	973.7	9.20	117.8	225.9	0.891	24.16	21.6	232	40.90
0.46	98.86	1.02	1.11	142.8	671.5	10.97	151.5	154.7	0.178	21.98	23.32	293.1	27.65
0.45	99.19	1.02	1.12	201.9	964.6	14.12	157.5	230.3	0.287	38.49	25.34	340.7	47.4
0.55	98.62	1.00	1.13	216.5	899.7	11.74	114.5	207.1	0.956	19.01	23.56	321	67.78
0.64	99.95	1.02	1.17	287.5	1150.5	13.68	151.3	313.1	0.741	33.99	22.69	322.3	112.3
0.56	99.20	0.99	1.20	440.7	1995.3	29.61	223.9	417.2	1.91	110.7	23.03	324.7	244.6
0.64	99.18	1.02	1.12	43.6	856.2	5.00	178.7	182.7	0.662	35.82	24.14	334.2	24.05
0.51	99.65	1.02	1.12	86.7	784.7	5.74	157.3	169	0.599	31.65	25.19	304.4	24.56
0.66	99.09	1.01	1.38	543.5	2332.1	46.34	149.8	357.3	4.92	30.54	19.32	147.3	320.8
0.33	98.57	1.02	1.36	412.3	2084.5	29.99	116.9	298.3	4.12	64.24	18.53	136.1	268
0.62	98.63	1.02	1.39	440.1	2284.6	33.93	137.2	328.2	4.37	57.39	18.82	140	285.7
0.75	99.58	1.02	1.37	436.8	2336.4	33.42	167.9	341	4.78	43.50	18.23	139.7	270.1
1.66	98.62	0.91	1.43	1008	3359	71.65	256.6	530	8.93	44.20	19.43	147.2	423.1
0.66	99.41	1.01	1.14	256.5	1141.2	12.74	231.2	307	1.35	24.56	22.17	274	59.86
0.62	98.83	1.02	1.10	194.6	865.8	12.68	163.1	448.8	0.317	40.42	18.31	164.5	53.50
0.47	98.72	1.00	1.09	174.9	1043.3	11.12	94.6	587.3	0.289	61.97	18.87	171	58.72
0.47	99.92	1.01	1.09	227.4	1107.4	12.91	117	527.2	0.341	58.77	20.04	189.1	59.53
0.60	98.03	1.01	1.26	352.3	1713.7	27.58	150.2	406.8	2.45	27.18	17.48	177.7	302.7
0.57	99.43	1.02	1.28	342.9	1450.9	23.25	104.4	354.7	2.42	32.31	18.39	197.5	299.1
0.57	98.89	1.01	1.25	362.6	1623.3	26.9	126	380.2	2.37	26.48	16.93	189.2	293.7
0.71	98.77	1.01	1.27	378.9	1550.7	27.62	138.2	376.8	2.44	32.71	16.94	183.3	282.7
0.60	98.89	1.00	1.26	361	1518.1	22.15	139	339.6	1.82	22.3	16.69	182.3	282.6
0.62	98.31	1.00	1.26	391.2	1655.4	26.01	109.8	379.2	2.56	21.42	17.35	174.3	280.7
0.38	99.14	1.02	1.28	370.9	1596.4	26	151.7	380.6	2.09	19.56	17.31	206.7	285.6
0.44	98.50	1.01	1.25	313.3	1590.7	17.6	122.4	380.7	1.78	217.1	16.46	203.7	261.1
				523.7	6293.7	264	82.3	1316.6	43.5	87.20	17.9	19.8	195
				567.3	6353.6	262	93	1239.1	44	77.00	20	20	194

(continued on next page)

tainties were expressed as $2\sigma_m$. Four measurements on the Sr standard NBS987 and the Nd standard LaJolla gave $^{87}Sr/^{86}Sr = 0.710234 \pm 7$ (2σ) and $^{143}Nd/^{144}Nd = 0.511838 \pm 8$ (2σ), respectively.

5. Zircon U–Pb geochronology

As shown in Fig. 3, all zircons from the five plutons exhibit well-developed oscillatory zoning indicating a magmatic origin. Because the oscillatory zoning is well-preserved through to the margin of the zircon, recrystallization, if any, is negligible. Except those from the Xiaochengzi (WL53063) and some zircons from the Maanzi (LW97066), most zircons do not contain a xenocrystic core.

U–Pb isotope analytical results are shown in Table 3 and the concordia diagrams (Figs. 4 and 5). Six fractions of zircon separate LW97077 (Longtoushan 1) are concordant within error (Fig. 4(a)). They yield a weighted mean $^{206}Pb/^{238}U$ age of 226.2 ± 3.9 Ma, with MSWD of 5.2. This age represents the time of emplacement for the Longtoushan 1 pluton. It reveals the Triassic granitoid plutonism after the amalgama-

Table 2 (*continued*)

Pluton/suite	Sample no.	Y	Zr	Nb	Cs	Ba	La	Ce	Pr	Nd	Sm	Eu	Gd	Tb
Maanzi Suite 2	WL852651	131.3	195.6	79.76	26.83	0.364	27.74	69.1	9.08	32.91	9.27	0.099	11.2	2.3
	WL852652	57.1	226.7	27.78	13.57	155.6	56.06	113.7	13.26	47.21	9.25	0.441	8.82	1.62
	WL852653	63.15	141.6	36.91	13.81	0.497	29.14	68.53	8.64	30.5	6.84	0.126	7.08	1.39
	WL852654	30.92	150.2	22.79	8.12	115.1	27.24	55.93	6.83	24.44	4.67	0.447	4.55	0.802
	WL852655	41.61	222.7	22.74	10.69	114.8	37.93	79.52	9.62	33.9	6.57	0.392	6.36	1.09
	WL852656	31.04	112.7	27.31	6.05	12.1	19.92	45.2	5.49	18.54	3.99	0.194	3.64	0.731
	LW97064	55.95	247.7	26.73	14.29	64.5	53.99	110.8	13.33	45.5	8.26	0.332	6.94	1.32
	LW97064-1	38.17	120.3	24.24	10.55	2.35	31.16	67.8	8.47	28.63	5.46	0.142	4.49	0.878
	LW97065	41.14	135.7	20.31	9.09	53.67	33.84	71.1	8.16	26.87	5.03	0.28	4.26	0.846
	LW97066	32.87	113.8	21.24	9.36	80.36	28.17	61.72	6.98	23.18	4.59	0.321	3.93	0.767
Yelaigai Suite 2	WL60421	52.2	168.4	16.44	11.69	105.1	29.59	68.65	9.1	35.65	8.72	0.215	8.97	1.4
	WL60422	68.13	226	18.96	11.43	257.8	48.15	106.7	13.55	54.66	12.52	0.396	12.37	2.08
	WL60423	57.25	174.4	13.28	10.61	266.1	35.02	75.87	9.8	37.34	8.59	0.447	7.78	1.4
	WL60424	48.9	204	14.2	23.38	342.4	37.64	80.03	9.97	37.89	7.26	0.468	6.66	1.09
	WL60425	45.45	286.9	15.85	28.1	651.5	40.76	83.09	10.37	36.47	6.8	0.683	5.94	0.978
	LW97079	64.44	195.6	17.23	15.54	107.6	33.76	77.2	10.56	42.02	9.96	0.188	10.52	1.76
	LW97080	63.93	184.7	17.19	13.22	103.4	35.11	80.69	10.65	44.16	10.52	0.202	11.54	1.96
Longtoushan 1 Suite 1	WL60420	12.48	202.8	6.33	5.4	590.5	22.66	43.81	5.18	19.19	3.45	0.75	3.04	0.412
	LW97076	10.56	137.6	5	5.2	520.2	21.63	40.51	4.72	17.72	2.9	0.648	2.19	0.332
	LW97077	12.18	155.9	5.64	5.97	511.6	22.83	43.41	5.13	18.76	3.38	0.69	2.77	0.367
	LW97078	10.85	204.9	5.63	6.3	556.6	22.19	41.3	4.8	17.17	3.3	0.625	2.37	0.375
	VII07B	19.41	183.1	8.63	6.64	644.4	30.75	60.14	7.08	25.39	4.71	0.845	3.62	0.583
Longtoushan 2 Suite 2	WL60428	41.58	259.7	30.37	9.93	157.3	42.35	92.96	10.39	35.78	6.91	0.413	6.11	1.13
	WL60429	33.2	201.6	14.36	5.04	373.4	34.11	66.59	8.67	34.26	6.5	0.256	5.75	0.929
	LW97019	36.12	243.4	13.67	7.46	385.9	55.36	106.5	13.03	48.15	8.11	0.245	6.67	1.1
	LW97020	35.93	268.1	17.19	8.57	405.8	50.07	99.64	11.96	45.02	7.98	0.315	6.21	1.02
Xiaochengzi Suite 1	WL53063	21.4	218.8	9.43	12.94	988.4	31.91	61.07	7.34	26.41	4.43	0.83	4.31	0.624
	WL53064	20.8	210.2	9.45	14.16	937.9	32.45	66.62	7.13	25.63	4.28	0.789	3.58	0.574
	WL53065	16.93	217.3	8.85	15.35	927.7	31.79	63.45	7.1	24.77	3.99	0.811	3.49	0.521
	WL53066	16.42	218.3	8.09	15.11	909.9	30.28	59.86	6.49	22.99	3.65	0.727	3.01	0.495
	WL53068	18.12	213.5	8.81	14.62	873.6	29.97	59.03	6.87	24.18	4.01	0.776	3.42	0.553
	WL53069	16.94	250.5	9.88	8.41	852.8	39.44	75.08	8.31	29.17	4.4	0.753	3.18	0.509
	WL53070	18.42	210	10.2	11.43	849.1	34.59	66.46	7.52	25.24	4.21	0.797	3.24	0.557
	LW97016	17.43	175.6	8.99	12.68	852.2	25.01	47.36	5.77	20.75	3.69	0.64	2.92	0.477
This study	W-2	22.7	96.3	8.5	0.99	177	10.6	24.1	3.15	13.1	2.98	0.93	3.58	0.65
Recommended[b]	W-2	23	94	7.8	0.99	173	10	23.5	3.20	14	3.25	1.01	3.60	0.63

tion of the Xingmeng with the Altaid. Five fractions of LW97066 (Maanzi) are concordant within error (Fig. 4(b)). Four fractions excluding fraction 3 yield a weighted mean $^{206}Pb/^{238}U$ age of 148.7 ± 2.1 Ma with MSWD of 2.1. Zircons of these four fractions are dominantly prismatic, the pyramidal form being less developed (Figs. 3(c) and (d)). Fraction 3 is distinct from the above four fractions on the concordia diagram, yielding a slightly older $^{206}Pb/^{238}U$ age of 158.4 Ma. This fraction exhibits well-developed pyramidal form and wide oscillatory-zoned bands (Fig. 3(e)), and either occurs as individual crystal or is enclosed within the prismatic zircon (Fig. 3(f)). Considering that country rocks of the Linxi granitoids are dominantly Permian sedimentary rocks, zircons of fraction 3 were probably not assimilated from the Jurassic volcanic rocks. In addition, this zircon fraction shows a relatively small length-to-width ratio ranging from ~1.7 to 3. Oscillatory zoning instead of sector zoning is developed within them. These features suggest a deep-seated, slow-cooling setting, instead of an eruptive, rapid-cooling setting, for their crystallization (Hoskin and Schaltegger, 2003). Therefore, we infer that zircons of fraction 3 contain a population inherited from the source rock. The age of 158.4 Ma

Dy	Ho	Er	Tm	Yb	Lu	Hf	Ta	Pb	Th	U	Eu/Eu*	$(La/Yb)_N$	Sr/Y
17.08	3.98	12.44	2.25	15.38	2.70	11.38	6.56	28.94	68.21	6.50	0.03	1.22	0.04
10.29	2.20	6.35	1.06	6.95	1.13	8.23	3.32	12.89	46.71	6.50	0.15	5.44	1.02
9.13	2.16	6.81	1.17	8.30	1.41	6.87	3.69	24.58	69.15	35.43	0.05	2.37	0.14
5.0	1.12	3.34	0.566	4.11	0.749	5.59	3.45	16.57	36.26	5.35	0.29	4.47	1.87
7.13	1.48	4.41	0.754	5.03	0.876	7.04	1.56	11.31	43.73	3.77	0.18	5.08	1.21
5.1	1.05	3.42	0.604	4.34	0.786	4.84	4.17	15.15	46.5	4.17	0.15	3.09	0.63
9.16	1.93	5.97	0.972	6.50	1.17	8.42	1.97	18.74	63.56	7.62	0.13	5.60	0.70
6.26	1.39	4.21	0.733	5.24	0.979	5.39	2.97	22.17	55.75	7.09	0.09	4.01	0.42
5.59	1.23	3.72	0.613	4.33	0.792	5.09	2.32	18.60	36.2	4.87	0.18	5.27	0.85
5.06	1.09	3.17	0.554	3.85	0.655	3.69	2.29	21.75	32.32	3.44	0.23	4.93	1.24
8.94	1.87	5.30	0.854	5.41	0.981	6.40	1.37	16.84	39.53	4.96	0.07	3.69	0.53
12.7	2.60	6.99	1.06	6.69	1.05	8.25	1.62	17.46	25.81	3.91	0.10	4.85	0.70
9.06	1.98	5.75	0.957	6.85	1.08	6.77	1.65	18.55	34.88	5.14	0.16	3.45	1.18
6.94	1.52	4.67	0.879	6.12	1.14	7.47	1.82	21.71	42.11	6.29	0.20	4.15	2.30
6.47	1.43	4.51	0.803	5.71	1.12	8.99	2.37	18.80	26.35	5.88	0.32	4.81	5.38
11.32	2.25	6.53	0.988	6.19	1.05	7.81	1.13	30.91	34.89	6.31	0.06	3.68	0.37
12.26	2.50	6.89	1.06	6.60	1.12	6.77	1.54	30.60	36.5	4.80	0.06	3.59	0.38
2.34	0.432	1.10	0.165	1.12	0.184	5.47	0.783	15.58	17.02	2.04	0.69	13.65	25.71
1.78	0.338	0.894	0.132	0.916	0.146	4.25	0.376	26.15	13.61	2.21	0.76	15.92	25.38
2.05	0.397	1.04	0.155	0.989	0.145	4.34	0.546	24.93	13.93	1.82	0.67	15.56	23.46
1.84	0.338	0.837	0.124	0.868	0.143	5.18	0.488	17.99	13.52	1.84	0.65	17.24	24.89
3.4	0.670	1.88	0.283	2.06	0.379	4.69	0.884	13.52	19.21	3.82	0.60	10.07	21.80
7.07	1.52	4.60	0.75	5.19	0.888	8.89	3.36	16.46	47.6	5.06	0.19	5.50	1.44
5.86	1.17	3.38	0.524	3.44	0.637	6.91	1.47	11.89	19.69	3.36	0.13	6.69	1.61
6.33	1.32	3.46	0.55	3.63	0.625	7.54	1.23	16.59	21.54	4.70	0.10	10.28	1.63
6.29	1.27	3.68	0.57	3.75	0.696	8.34	1.34	19.37	22.45	3.53	0.13	8.99	1.66
3.69	0.775	2.11	0.343	2.29	0.428	6.65	1.00	17.26	28.51	2.72	0.57	9.39	14.14
3.53	0.755	2.12	0.34	2.28	0.453	6.87	1.02	42.45	25.59	2.61	0.60	9.60	14.38
2.86	0.601	1.67	0.255	1.80	0.323	6.47	0.684	22.19	27.65	2.69	0.65	11.93	17.35
2.7	0.601	1.55	0.268	1.81	0.318	6.49	0.917	17.90	23.29	2.42	0.65	11.27	17.22
3.01	0.638	1.66	0.276	1.95	0.336	6.29	0.717	15.57	27.37	2.57	0.63	10.35	15.60
2.92	0.573	1.61	0.252	1.76	0.343	7.10	1.27	13.93	39.21	3.17	0.59	15.09	16.57
3.0	0.657	1.79	0.257	2.00	0.371	6.53	1.41	15.81	33.46	3.31	0.64	11.65	15.50
2.84	0.603	1.68	0.259	1.84	0.34	5.84	1.23	14.00	29.64	3.19	0.58	9.15	14.98
3.91	0.81	2.20	0.35	2.08	0.32	2.47	0.49	9.98	2.36	0.54			
3.80	0.76	2.40	0.38	2.05	0.33	2.40	0.50	8.77	2.2	0.53			

probably represents that of the source rock. It is noteworthy that the zircon cores are euhedral without a subrounded surface, and that the zircon rims keep the same crystallographic orientation (Fig. 3(f)). These features suggest that re-melting of the source rock soon followed its formation without a sharp interruptive temperature drop. Five fractions of WL60423 (Yelaigai) define a discordia line with a negative lower concordia age (Fig. 4(c)). This line represents the lead loss line (Davis and Krogh, 2000). The upper intercept age of 147.5 ± 1.3 Ma, with MSWD of 0.009, is actually identical to that of the Maanzi pluton. Both ages represent the time of granite magmatism, concurrent with or, strictly speaking, soon following the extensive Late Jurassic volcanism.

Five fractions of WL60428 (Longtoushan 2) are clustered on the concordia diagram (Fig. 5(a)). They yield a weighted mean $^{206}Pb/^{238}U$ age of 117.3 ± 3.9 Ma with MSWD of 4.4. Fraction 2 of WL53063 (Xiaochengzi) is concordant (Fig. 5(b)). Zircons of fraction 2 are acicular or long-prismatic without a xenocrystic core (Fig. 3(k)). Its concordant $^{206}Pb/^{238}U$ age of 111 Ma represents the time of emplacement for this pluton. However, a majority of zircons from WL53063 contain a dark, subrounded xenocrystic

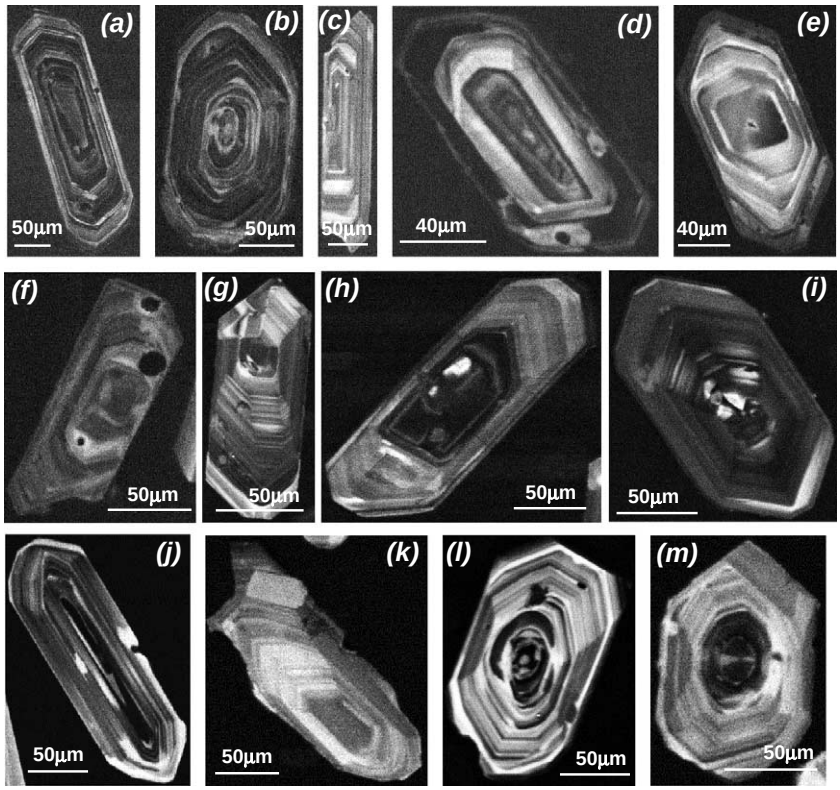

Fig. 3. Cathodoluminescence photographs showing the petrographic characteristics of zircon populations from the Longtoushan 1 (LW97077) ((a) and (b)), the Maanzi (LW97066) ((c)–(f)), the Yelaigai (WL60423) ((g) and (h)), the Longtoushan 2 (WL60428) ((i) and (j)), and the Xiaochengzi (WL53063) ((k)–(m)). The pyramidal zircon (e) and its occurrence as the core within a prismatic zircon (f), and the dark, subrounded xenocrystic cores ((l) and (m)) are noteworthy.

core in various proportions. These xenocrystic cores also show oscillatory zoning again suggesting a magmatic origin (Figs. 3(l) and (m)). Four fractions from WL53063 define a discordia line. The lower intercept age of 110.5 ± 1.1 Ma, with MSWD of 0.61, is identical with that of fraction 2. The upper intercept age of 1124 ± 32 Ma represents the age of the xenocrystic core. Because country rocks of the Xiaochengzi pluton are the Upper Permian and the Lower Permian, these xenocrystic cores are inherited from the source rock. The age and the oscillatory zoning of the xenocrystic cores reveal the presence of the Proterozoic orthogneiss in the basement or the lower crust. It is stressed that emplacement ages of the Longtoushan 2 and the Xiaochengzi plutons represent the time of intrusion of voluminous granites and eruption of rhyolite tuff within the Great Xing'an Mountains.

6. Major element and trace element compositions

Major element and trace element analytical data are shown in Table 2. As shown in Fig. 6, all the data have Alumina Saturation Index (A/NKC) less than 1.05, suggesting an igneous protolith (Chappell, 1999). Although Suites 1 and 2, except data of VII07B, are indistinguishable in A/NKC values, Suite 1 displays distinctly higher A/NK values than Suite 2. These characteristics confirm the petrograghic observation that the total amount of feldspar in the rock varies little between Suites 1 and 2, but the amount of alkali feldspar tends to be much greater in Suite 2 (Table 1). As shown in Fig. 7, all the data of Suite 2 plot in the field of A-type granites, whereas the data of Suite 1, except one on the rectangular frame, plot within the field for the other types. So, Suites 1 and 2 correspond to I- and A-types, respectively.

Table 3
Zircon U–Pb isotopic data[a]

Sample (fraction)	Pluton (Suite) Petrographic Description	Sample weight (μg)	$^{206}Pb/^{204}Pb$	U (ppm)	Pb (ppm)	Pb* (ppm)	Atomic ratios			$^{207}Pb^*/^{235}U$	± 2σ	$^{207}Pb^*/^{206}Pb^*$	± 2σ	Apparent ages (Ma)			Rho
							$^{208}Pb^*/^{206}Pb^*$	$^{206}Pb^*/^{238}U$	± 2σ					$^{206}Pb^*/^{238}U$	$^{207}Pb^*/^{235}U$	$^{207}Pb^*/^{206}Pb^*$	
LW97077	*Longtoushan 1 (Suite 1)*																
(1)	39 grains, yellowish, prismatic, fragments	70.4	1166	1119	38.7	38.5	0.0921	0.034998	0.000539	0.24408	0.00378	0.050581	0.000095	221.8	221.8	221.8	0.990347
(2)	21 grains, medium-sized, yellowish, prismatic	133.2	3118	1361	50.0	49.9	0.0924	0.037312	0.000895	0.26185	0.00628	0.050898	0.000058	236.2	236.2	236.2	0.999003
(3)	37 grains, transparent, long-prismatic or acicular	81.8	2753	1283	45.5	45.4	0.108	0.035550	0.000377	0.24830	0.00268	0.050656	0.000132	225.2	225.2	225.2	0.986505
(4)	18 grains, transparent, prismatic	43.1	290.3	818	30.9	29.4	0.103	0.036269	0.000754	0.25383	0.00536	0.050757	0.000165	229.7	229.7	229.8	0.988044
(5)	36 grains, small, transparent, stubby	24.4	334.3	841	29.3	28.9	0.0795	0.035321	0.000523	0.24656	0.00530	0.050628	0.000487	223.8	223.8	223.9	0.908919
(6)	32 grains, small, yellowish, stubby	97.5	1604	1037	37.2	37.1	0.103	0.036036	0.000386	0.25204	0.00275	0.050727	0.000119	228.2	228.2	228.4	0.990132
LW97066	*Maanzi (Suite 2)*																
(1)	36 grains, small, yellowish, prismatic	32.5	1575	3968	89.6	88.5	0.0727	0.023134	0.000248	0.15627	0.00172	0.048992	0.000161	147.4	147.4	147.4	0.974598
(2)	20 grains, yellowish, prismatic, fragments	56.3	2958	2558	59.4	59.2	0.0925	0.023559	0.000254	0.15932	0.00174	0.049049	0.000088	150.1	150.1	150.2	0.992645
(3)	13 grains, medium-sized, transparent, pyramidal	18.5	450.8	2087	52.3	51.6	0.107	0.024876	0.000378	0.16884	0.00304	0.049225	0.000418	158.4	158.4	158.6	0.926791
(4)	17 grains, transparent, prismatic, fragments	20.0	218.8	660	16.2	15.5	0.113	0.023511	0.000496	0.15898	0.00418	0.049043	0.000750	149.8	149.8	149.9	0.893656
(5)	23 grains, medium-sized, yellowish, prismatic	43.7	2121	3545	80.4	79.7	0.0771	0.023261	0.000254	0.15719	0.00173	0.049009	0.000159	148.2	148.2	148.3	0.987826
WL60423	*Yelaigai (Suite 2)*																
(1)	41 grains, large, yellowish, prismatic, fragments	60.0	1574	3334	70.4	69.7	0.0670	0.021773	0.000229	0.14716	0.00156	0.049020	0.000031	138.9	139.4	148.8	0.998203
(2)	59 grains, small, yellowish, prismatic	43.2	2030	3454	77.6	75.2	0.0784	0.022465	0.000234	0.15180	0.00158	0.049007	0.000036	143.2	143.5	148.2	0.997486
(3)	28 grains, large, transparent, prismatic, fragments	56.2	1041	1323	25.9	24.4	0.0883	0.018881	0.000204	0.12780	0.00138	0.049091	0.000044	120.6	122.1	152.2	0.996583
(4)	51 grains, small, transparent, prismatic	62.4	1023	1266	28.1	26.4	0.0931	0.021257	0.000215	0.14372	0.00147	0.049034	0.000043	135.6	136.4	149.5	0.996207
(5)	53 grains, medium-sized, yellowish, prismatic, fragments	39.5	1058	2532	55.2	52.0	0.0818	0.021109	0.000215	0.14271	0.00146	0.049033	0.000039	134.7	135.5	149.4	0.997041
WL60428	*Longtoushan 2 (Suite 2)*																
(1)	30 grains, medium-sized, orange yellowish, prismatic	39.6	331.8	413	8.03	7.54	0.126	0.018057	0.000337	0.12032	0.00243	0.048327	0.000349	115.4	115.4	115.3	0.924803
(2)	31 grains, medium-sized, pale yellowish, prismatic	46.6	243.8	679	13.4	12.8	0.135	0.018466	0.000600	0.12317	0.00579	0.048379	0.001567	118.0	118.0	117.8	0.704900
(3)	61 grains, small, transparent, prismatic or acicular	17.7	169.8	805	16.0	14.9	0.147	0.018031	0.000578	0.12014	0.00475	0.048322	0.001108	115.2	115.2	115.1	0.841950
(4)	32 grains, small, pale yellowish, prismatic	42.5	194.9	500	10.2	9.89	0.142	0.019303	0.000510	0.12905	0.00548	0.048490	0.001422	123.3	123.2	123.2	0.736670
(5)	175 grains, small, yellowish, prismatic or stubby	30.0	227.1	861	17.2	16.7	0.152	0.018357	0.000441	0.12242	0.00312	0.048365	0.000598	117.3	117.3	117.1	0.945692
WL53063	*Xiaochengzi (Suite 1)*																
(1)	41 grains, large, transparent, stubby	46.5	374.2	461	11.7	11.6	0.132	0.024602	0.000251	0.19554	0.00209	0.057647	0.000182	156.7	181.4	516.4	0.936526
(2)	41 grains, medium-sized, transparent, acicular or prismatic	49.8	377.1	598	10.6	10.6	0.134	0.017365	0.000179	0.11546	0.00127	0.048225	0.000175	111.0	111.0	110.3	0.911051
(3)	37 grains, large, yellowish, stubby	39.0	214.2	441	9.76	9.16	0.137	0.020273	0.000215	0.14808	0.00176	0.052977	0.000278	129.4	140.2	327.8	0.879760
(4)	61 grains, small, yellowish, stubby or prismatic	34.6	208.3	757	13.8	13.3	0.117	0.017497	0.000192	0.11770	0.00138	0.048788	0.000188	111.8	113.0	137.7	0.868770

The $^{206}Pb/^{204}Pb$ ratios are measured values. Row analytical data were calculated with the 'Pbdat' program of Ludwig (1988).

[a] Concentrations of U and Pb are calculated with the zircon weight.

As illustrated in Figs. 8 and 9, Suites 1 and 2 of the Linxi granitoids plot within distinct fields. However, sample WL60425 from the Yelaigai of Suite 2 plots within the field of Suite 1, but is distinct from the rest samples of Suite 2 so as to form an obvious gap (Fig. 8). Suite 1 tends to show lower SiO_2 and K_2O contents, and higher Al_2O_3, CaO, MgO, FeO, TiO_2, and P_2O_5 than Suite 2 (Table 2 and Fig. 8). In both suites, $CaO+Na_2O$, P_2O_5, $MgO+FeO$, and TiO_2 tend to decrease with increasing SiO_2. However, K_2O tends to increase, or decrease, with increasing SiO_2 for Suites 1 and 2, respectively. It is noteworthy that in Figs. 8(b) and (e), the data of Suite 2, notably the Maanzi pluton, are scattered. As shown in Fig. 9, Suite 1 shows higher Sr, Ba, and Eu abundances, and lower Sm+Gd, Nb, Y, and Yb than Suite 2. For each pluton from Suite 1 and the whole data set of Suite 2, Sr, Ba, and Eu decrease with increasing SiO_2. Sm+Gd, Nb, Y, and Yb decrease, or tend to increase, with decreasing Eu for Suites 1 and 2, respectively. These characteristics result in remarkably high and low La/Yb_N and Sr/Y ratios for Suites 1 and 2, respectively (Fig. 10). Nevertheless, the data of Suite 2 are much scattered (Figs. 9(d)–(g) and 10).

As shown in Fig. 11, Suite 1 shows relatively steep rare earth element (REE) patterns with moderate negative Eu anomalies. Large ion lithophile elements (LILE) are enriched relative to high-field-strength elements (HFSE), with notable depletions of Nb, Ti, and P, and moderate or minor depletion of Ba and Sr. As shown in Fig. 12, Suite 2 exhibits limited enrichment of light REE, pronounced and various negative Eu anomalies, and elevated heavy REE patterns. Both LILE and HFSE are generally enriched, with less obvious depletion in Nb and more pronounced depletion in Ba, Sr, P, and Eu than in Suite 1.

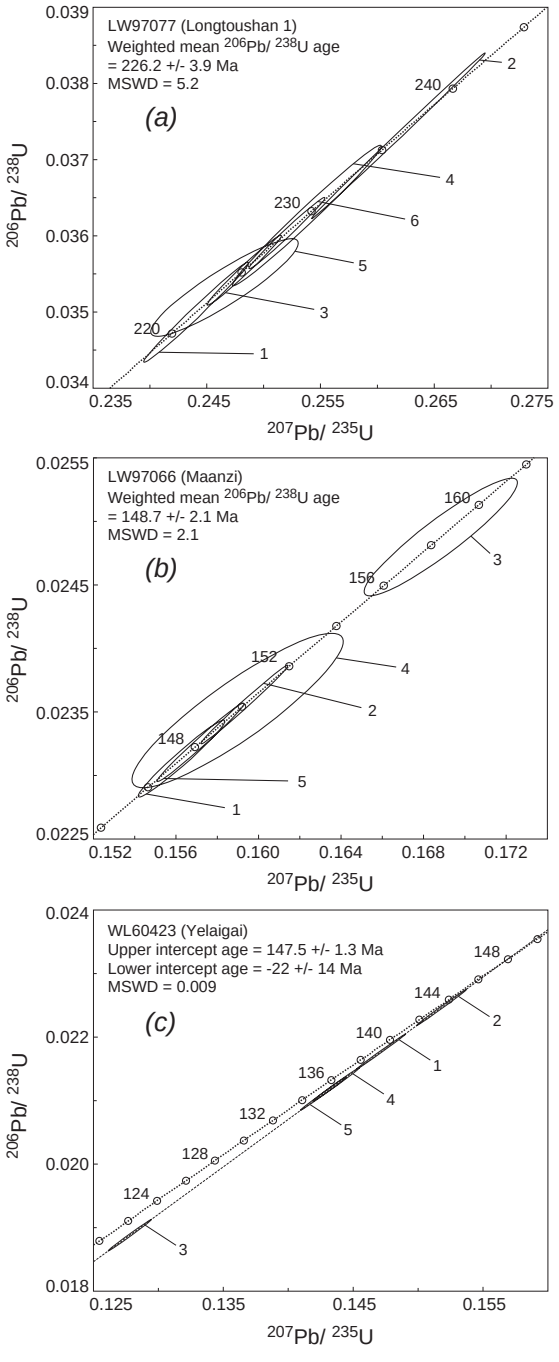

Fig. 4. $^{207}Pb/^{235}U$ vs. $^{206}Pb/^{238}U$ concordia diagrams for zircon separates LW97077 (Longtoushan 1) ((a)), LW97066 (Maanzi) ((b)), and WL60423 (Yelaigai) ((c)). Data of each fraction is shown as an error ellipse, with the fraction number indicated. The number and the dot on the concordia curve (dotted) represent the age (Ma). The dashed line in (c) represents the discordia line fitted with model 1 solution of Ludwig (1994). Weighted mean $^{206}Pb/^{238}U$ ages were calculated at 95% confidence, with fraction 3 excluded from the calculation for LW97066 (b).

7. Rb–Sr and Sm–Nd isotope compositions

Rb–Sr and Sm–Nd isotope analytical data are listed in Tables 4 and 5, respectively. Values of $(^{87}Sr/^{86}Sr)_t$, $(^{143}Nd/^{144}Nd)_t$, and $\varepsilon_{Nd}(t)$ were calculated at the

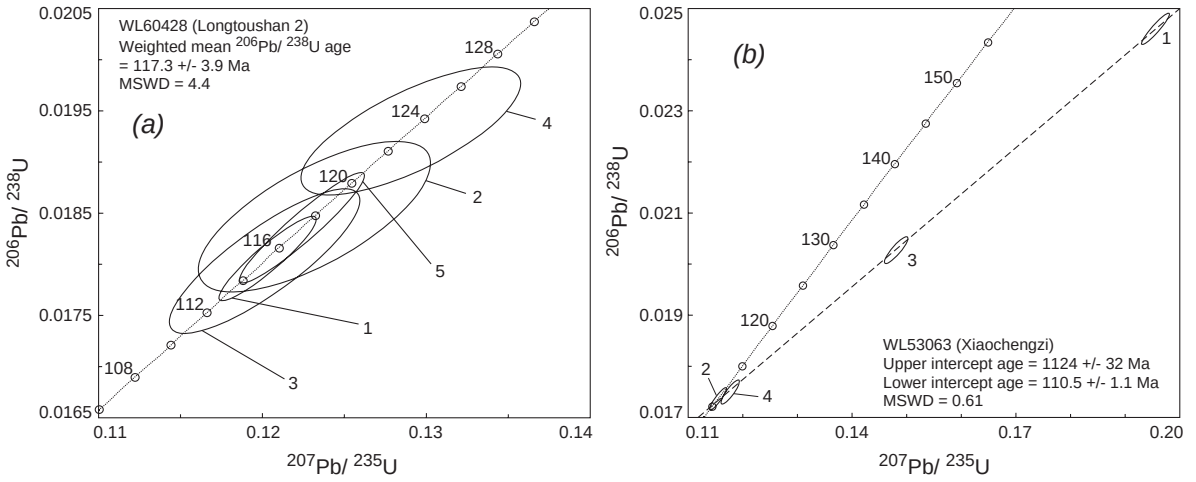

Fig. 5. $^{207}Pb/^{235}U$ vs. $^{206}Pb/^{238}U$ concordia diagrams for zircon separates WL60428 (Longtoushan 2) (a) and WL53063 (Xiaochengzi) (b). For explanation, see caption of Fig. 4.

emplacement age for granitoids, at 150 Ma for the Late Jurassic basalts, at 120 Ma for the Proterozoic gneisses, and at 230 Ma for the Early Permian mafic to intermediate eruptive rocks (Y.F. Zhu, unpublished data). Values $(^{87}Sr/^{86}Sr)_t$ of 32 granitoid samples vary from 0.701764 to 0.707654, and values $\varepsilon_{Nd}(t)$ of 29 granitoid samples vary from +5.60 to −2.89. The Xiaochengzi granitoids show the lowest negative $\varepsilon_{Nd}(t)$ values ranging between −1.88 and −2.89, whereas the Maanzi and the Longtoushan 1 granitoids have the highest positive $\varepsilon_{Nd}(t)$ values that vary from +5.45 to +4.06 and from +5.60 to + 3.01, respectively.

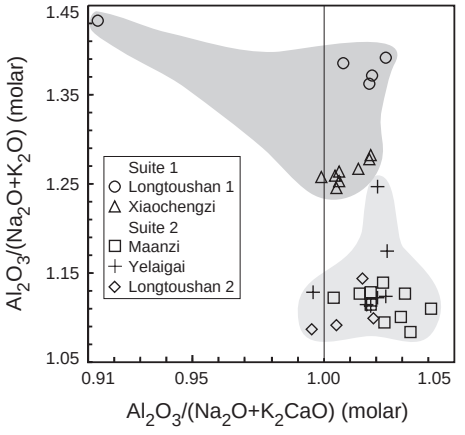

Fig. 6. A/NK vs. A/NKC diagram showing the metaluminous characteristic of Suites 1 and 2.

The Yelaigai and the Longtoushan 2 granitoids have intermediate $\varepsilon_{Nd}(t)$ values.

To evaluate the error in the determination of initial $(^{87}Sr/^{86}Sr)_t$ values, we calculated the error $\pm \Delta(^{87}Sr/^{86}Sr)_t$ that is caused by the analytical errors of both $\pm \Delta(^{87}Sr/^{86}Sr)$ and $\pm \Delta t$, and $\pm \Delta(^{87}Rb/^{86}Sr)$ and $\pm \Delta t$ (Table 4). Errors resulting from the latter are much greater than errors resulting from the former. Variation in $(^{87}Sr/^{86}Sr)_t$ within each pluton is comparable with the error $\pm \Delta(^{87}Sr/^{86}Sr)_t$, indicating that the variation largely stems from the analytical error $\pm \Delta(^{87}Rb/^{86}Sr)$. Suite 2 granitoids exhibit relatively large $^{87}Rb/^{86}Sr$ values as a result of extensive feldspar fractionation (see Section 8.2) and, hence, large $\pm \Delta(^{87}Sr/^{86}Sr)_t$ values. Therefore, Suite 2 shows more scattered $(^{87}Sr/^{86}Sr)_t$ values than Suite 1. Similarly, errors $\pm \Delta(^{143}Nd/^{144}Nd)_t$ and $\pm \Delta\varepsilon_{Nd}(t)$ were calculated (Table 5). However, variation in $\varepsilon_{Nd}(t)$ within each pluton is much greater than $\pm \Delta\varepsilon_{Nd}(t)$ caused by $\pm \Delta t$ and either $\pm \Delta(^{147}Sm/^{144}Nd)$ or $\pm \Delta(^{143}Nd/^{144}Nd)$. So, $\varepsilon_{Nd}(t)$ variations within and between plutons reflects heterogeneous $(^{143}Nd/^{144}Nd)_t$ compositions of the source region.

These results are comparable to the Nd and Sr isotope compositions of granitoids from the western and the eastern segments of the Central Asian Orogenic Belt. The western and the eastern Junggar, Xinjiang are the western segment of the belt. Late Paleozoic granitoids from the western Junggar have $\varepsilon_{Nd}(t)$ varying from +6.06 to +5.65, and $(^{87}Sr/^{86}Sr)_t$

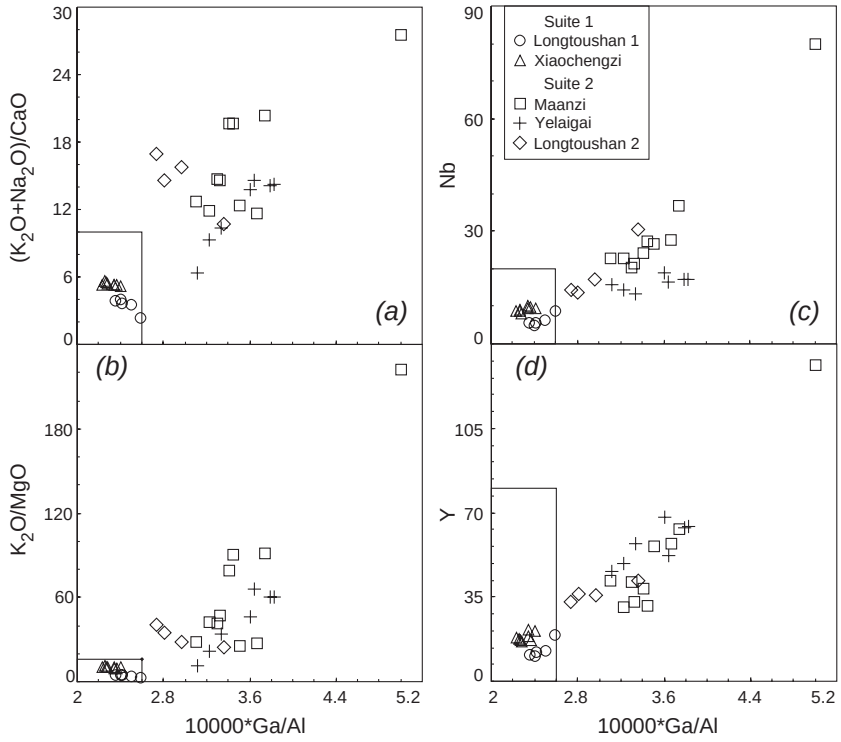

Fig. 7. Diagrams discriminating A-type granites from the other types of granites (after Whalen et al., 1987).

varying from 0.703715 to 0.704606 (He et al., 1994). Late Paleozoic A-type granites from the eastern Junggar have $\varepsilon_{Nd}(t)$ ranging from +6.67 to +5.06 (Han et al., 1997), and $(^{87}Sr/^{86}Sr)_t$ ranging from 0.701702 to 0.704464 (Liu, 1993; Han et al., 1997). Northeastern China is the easternmost segment of the Central Asian Orogenic Belt. In this region, Wu et al. (2000) distinguished two groups of Mesozoic granites on the basis of emplacement setting. The dominant Group I that occurs in the orogenic domain without Precambrian basement has $\varepsilon_{Nd}(t)$ varying from +3.96 to −3.45, and $(^{87}Sr/^{86}Sr)_t$ averaging 0.7048. The subordinate Group II that was emplaced within the Precambrian basement shows $\varepsilon_{Nd}(t)$ ranging from −6.27 to −7.36, and higher $(^{87}Sr/^{86}Sr)_t$ varying from 0.7094 to 0.7183. In summary, the Nd and Sr isotope compositions of granitoids within the Central Asian Orogenic Belt indicate a significant continental crust growth during the Paleozoic and the Mesozoic times.

In terms of the $\varepsilon_{Nd}(t)$ and $(^{87}Sr/^{86}Sr)_t$ values, the Linxi granitoids are intermediate between those from the western and the easternmost segments of the Central Asian Orogenic Belt. Granitoids from the western to the eastern segments of the belt tend to display increasingly lower $\varepsilon_{Nd}(t)$ and higher $(^{87}Sr/^{86}Sr)_t$ values. These variations suggest that increasingly greater amounts of continental crust materials are involved in the granitoid production towards the eastern part of the belt.

8. Discussion

8.1. Sources of heat and material for the production of the Linxi granitoids

As shown in Fig. 13(a), $\varepsilon_{Nd}(t)$ and $(^{87}Sr/^{86}Sr)_t$ values of the Linxi granitoids, the Early Permian and the Late Jurassic eruptive rocks, and the Proterozoic gneisses are broadly negatively correlated. For reasons shown below,

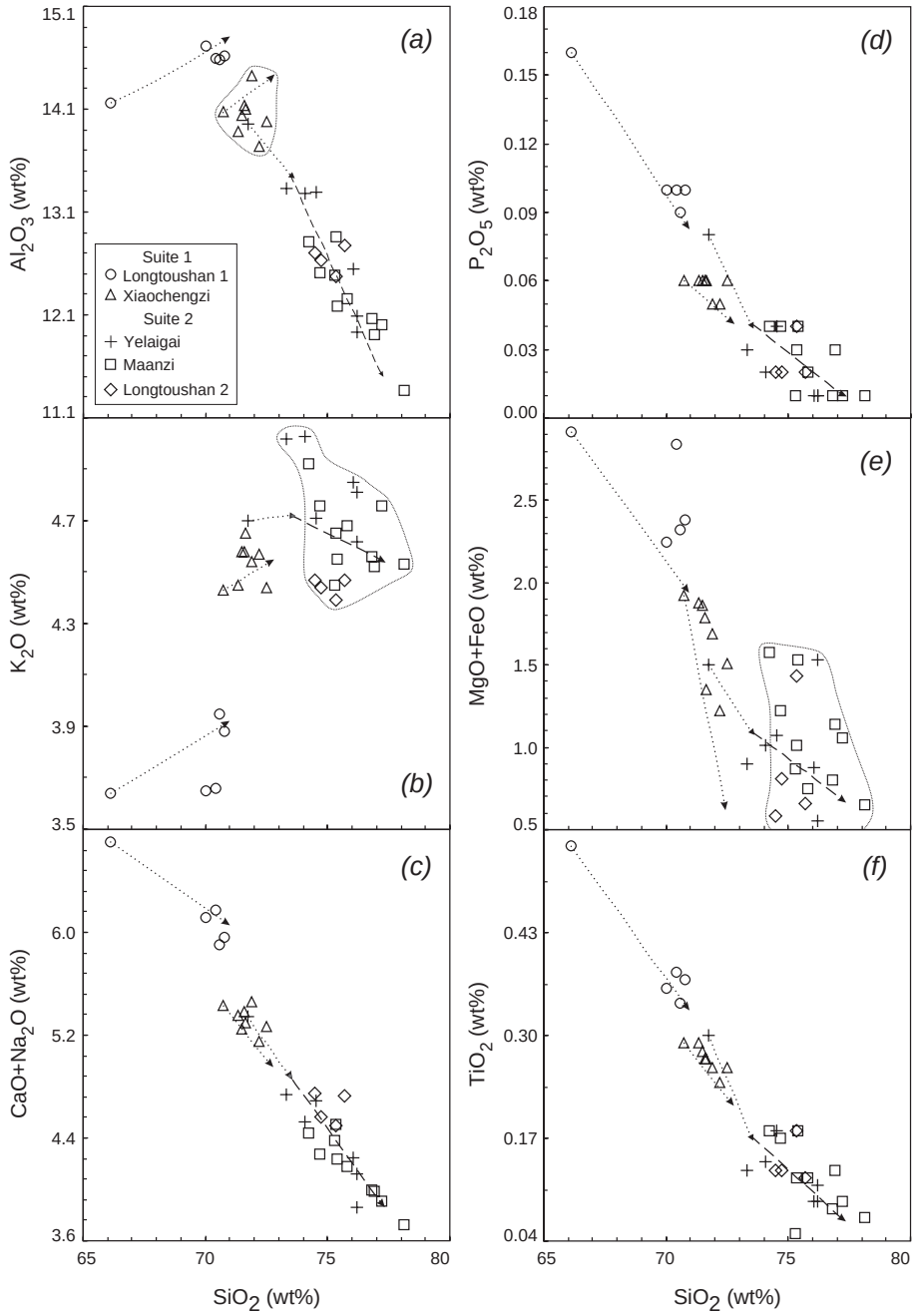

Fig. 8. Harker diagrams showing the major element variations of Suites 1 and 2. The fractionation trajectory starting from the parent magma towards the residual melt (arrow-head) was modeled to the data sets of the Longtoushan 1 (dotted), the Xiaochengzi (dotted), and Suite 2 (dotted for Step 1, and dashed for Step 2). For details of the modeling, see Table 6. The scattered data are circled.

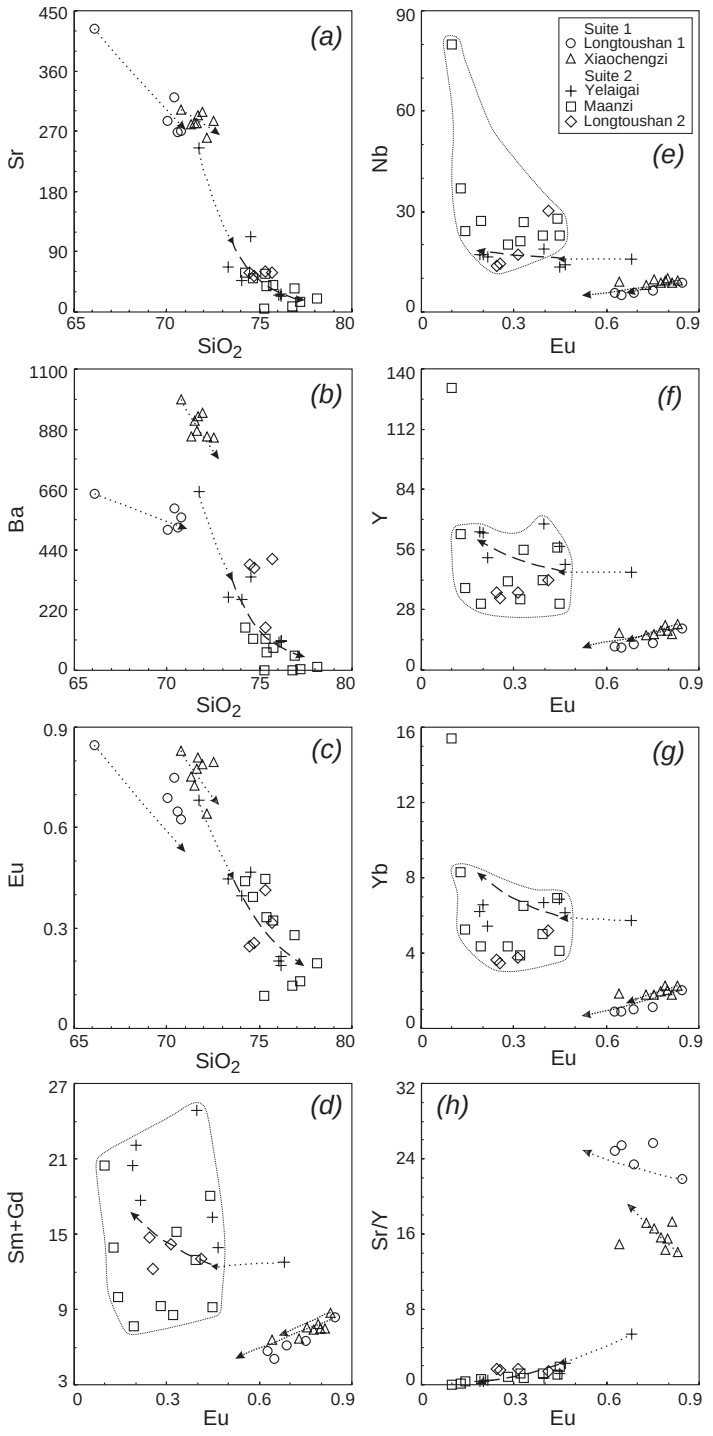

Fig. 9. Trace element vs. SiO_2 and Eu diagrams for Suites 1 and 2. The fractionation trajectory starting from the parent magma towards the residual melt (arrow-head) was modeled to the data sets of the Longtoushan 1 (dotted), the Xiaochengzi (dotted), and Suite 2 (dotted for Step 1, and dashed for Step 2). For details of the modeling, see Table 6. In (d)–(g), the scattered data of Suite 2 are circled.

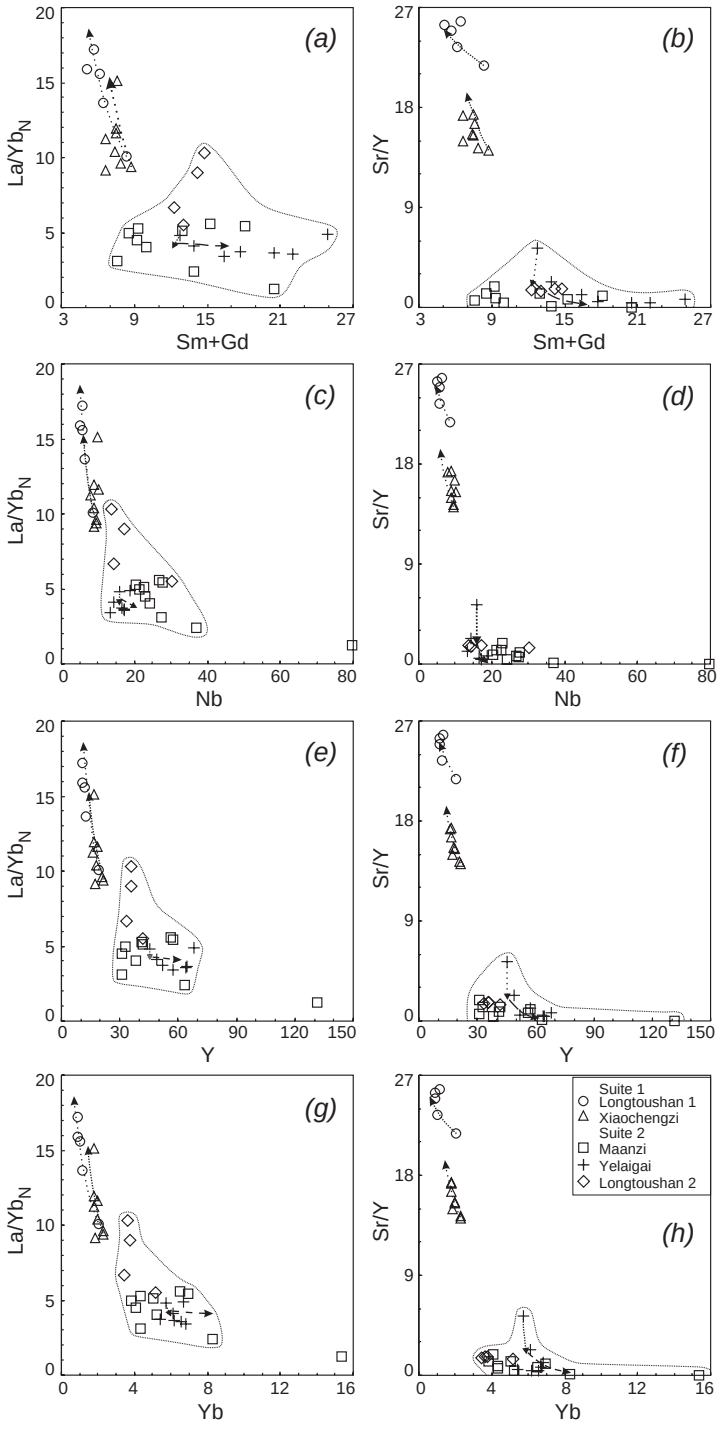

Fig. 10. La/Yb$_N$ and Sr/Y vs. Sm+Gd, Nb, Y, and Yb for the Linxi granitoids. The fractionation trajectory starting from the parent magma towards the residual melt (arrow-head) was modeled to the data sets of the Longtoushan 1 (dotted), the Xiaochengzi (dotted), and Suite 2 (dotted for Step 1, and dashed for Step 2). For details of the modeling, see Table 6. The scattered data of Suite 2 are circled.

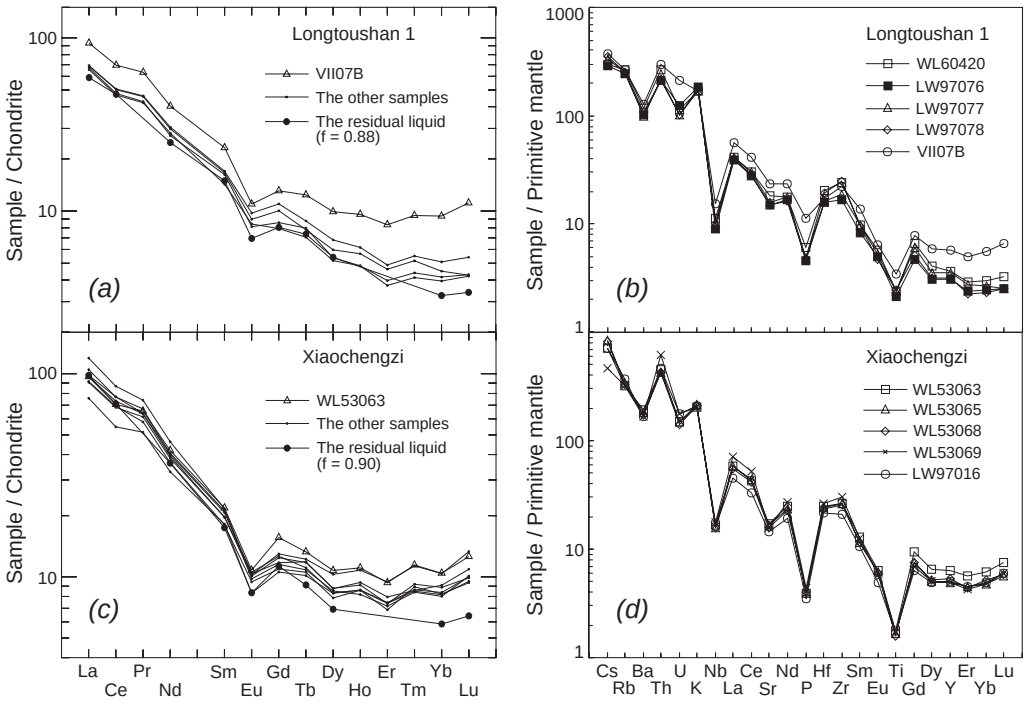

Fig. 11. REE-chondrite normalized (Nakamura, 1974) patterns ((a) and (c)), and the primitive mantle normalized multi-element diagrams ((b) and (d)) for Suite 1. The normalizing values of P and the rest elements for primitive mantle from Wood et al. (1979) and Taylor and McLennan (1985), respectively.

the AFC process is not considered to be responsible for the $\varepsilon_{Nd}(t)$ and $(^{87}Sr/^{86}Sr)_t$ variations. First, no detrital xenocrystic cores of zircon with old U–Pb isotope ages, which would have been assimilated from the country rock, were observed in the Linxi granitoids except the Xiaochengzi pluton. With regard to the Xiaochengzi pluton, as argued in Section 5, the xenocrystic zircon cores that yield the Proterozoic U–Pb isotope age derive from the source rock rather than were assimilated from the much younger Permian sedimentary country rocks. Second, with progressively greater amounts of crustal material assimilated, the magma would have more evolved and more scattered Sr and Nd isotopic compositions (DePaolo, 1981). However, $(^{87}Sr/^{86}Sr)_t$ and $\varepsilon_{Nd}(t)$ values of the Xiaochengzi granitoids that are high and the lowest, respectively, among the five plutons are clustered together (Fig. 13(a)).

Magma mixing tends to generate undercooled magmatic inclusions (Poli and Tommasini, 1991; Tepley et al., 2000). However, microdioritic enclaves occur rarely (< 1%) in the Longtoushan 1 pluton, and are scarce or absent from the other four plutons. Therefore, magma mixing is not the main cause of the negative $\varepsilon_{Nd}(t)$ vs. $(^{87}Sr/^{86}Sr)_t$ correlation for the Linxi granitoids.

A heterogeneous or mixed source composition between two endmembers was tested as the cause of the Sr and Nd isotope variation. Because sample S1805 from the Late Jurassic basalts has the highest $\varepsilon_{Nd}(t)$ value, it was chosen to represent the newly mantle-derived material. Xenocrystic cores of zircon from the Xiaochengzi pluton that show both oscillatory zoning and the Proterozoic U–Pb isotope age suggest the Proterozoic orthogneiss as the crustal component. Moreover, the relatively steep negative trend of the Linxi granitoids in Fig. 13(a) requires a crustal component with moderately negative $\varepsilon_{Nd}(t)$ at moderate $(^{87}Sr/^{86}Sr)_t$ values. The Proterozoic gneisses meet this requirement. So, the average $\varepsilon_{Nd}(t)$ and $(^{87}Sr/^{86}Sr)_t$ values of the five Proterozoic gneiss samples at 120 Ma were chosen to represent those of the crustal component. A hyperbola of simple mixing was constructed between these two endmembers. The Maanzi and the Longtoushan 1

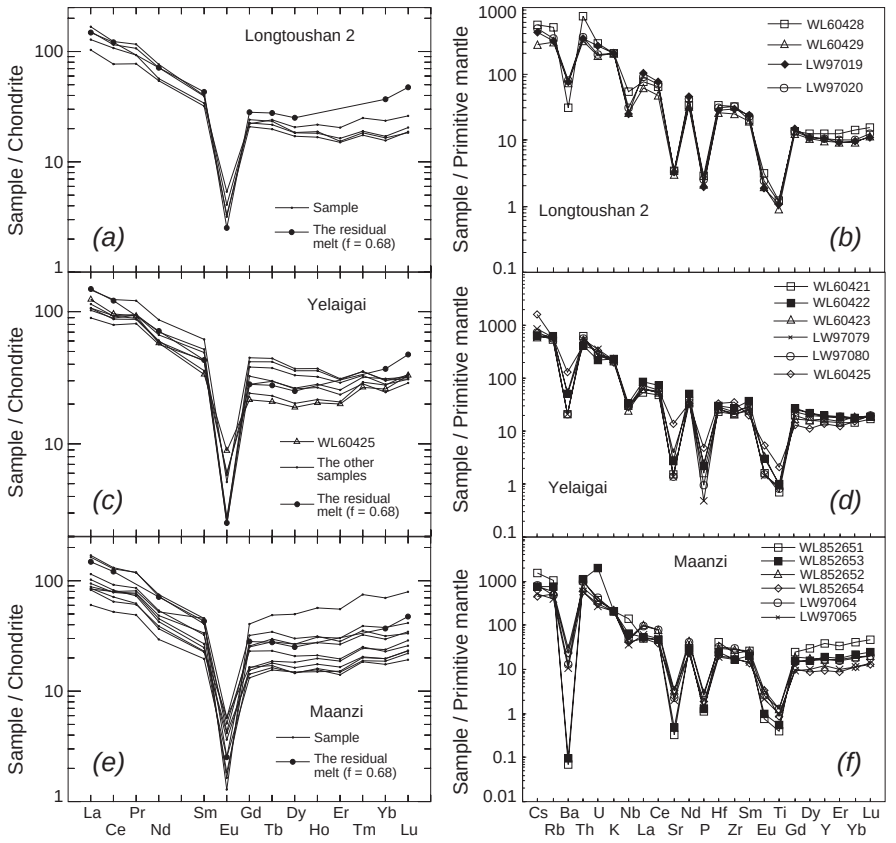

Fig. 12. REE-chondrite normalized (Nakamura, 1974) patterns (the left), and the primitive mantle normalized multi-element diagrams (the right) for Suite 2. Same sources of the normalizing values as in Fig. 11.

granitoids show similar $\varepsilon_{Nd}(t)$ and $(^{87}Sr/^{86}Sr)_t$ values as the Late Jurassic basalts and alkaline basalt. In addition, the $^{206}Pb/^{238}U$ age of 158.4 Ma for fraction 3 zircons from the Maanzi pluton indicates the Late Jurassic age for the source rock. Therefore, the underplated equivalents of the Late Jurassic basalts form the source rock for the Maanzi pluton. However, the Early Permian mafic to intermediate eruptive rocks show lower $\varepsilon_{Nd}(t)$ and more scattered $(^{87}Sr/^{86}Sr)_t$ values than the Longtoushan 1 granitoids. This discrepancy may result from greater amounts of crustal material mixed or assimilated into the former during melting or magma ascendance. The underplated equivalents of the Early Permian eruptive rocks that should have more primitive isotope compositions likely form the source rock for the Longtoushan 1 pluton. Alternatively, the Longtoushan 1 granitoids represent thoroughly blended magma. The rare occurrence of microdioritic enclaves within this pluton represents the vestige of magma mixing. In or near the source region, mantle-derived magmas would be directly introduced into the crustal melt resulting in thorough mixing (e.g., Cocherie et al., 1994). A continued underplating at the base of the lower crust through the Late Jurassic to the Early Cretaceous time provided prolonged heat supply to melt the earlier magma inputs. The Yelaigai and the Longtoushan 2 granitoids correspond to the segment of the mixing hyperbola between 0.9 and 0.8 fraction basalt, whereas the Xiaochengzi granitoids correspond to the segment between 0.7 and 0.6 fraction basalt. With the emplacement age becoming younger, the five plutons contain increasingly greater fractions of the lower-crustal component in addition to the underplated basaltic material. This implies that, with prolonged heating of the lower crust,

Table 4
Rb–Sr isotopic data

Pluton/suite	t (Ma)	Sample no.	Rb (ppm)	Sr (ppm)	$^{87}Rb/^{86}Sr$	$^{87}Sr/^{86}Sr$	$\pm 2\sigma_m$	$(^{87}Sr/^{86}Sr)_t$[a]	$\pm \Delta(^{87}Sr/^{86}Sr)_t$[b]	$\pm \Delta(^{87}Sr/^{86}Sr)_t$[c]
Maanzi Suite 2	148.7	WL852652	307.9	55.79	16.02	0.737023	8	0.703160	0.001166	0.000487
	148.7	WL852654	285.8	57.14	14.517	0.734201	8	0.703516	0.001056	0.000442
	148.7	WL852655	281.1	56.52	14.475	0.735858	9	0.705260	0.001053	0.000442
	148.7	WL852656	308	18.36	49.013	0.806008	13	0.702407	0.003566	0.001478
	148.7	LW97064	262.4	38.43	19.835	0.745483	12	0.703557	0.001443	0.000605
	148.7	LW97064-1	265	14.6	52.105	0.814093	11	0.703954	0.003791	0.001568
	148.7	LW97065	238.9	37.36	18.572	0.743131	2	0.703875	0.001351	0.000557
	148.7	LW97066	241.1	41.68	16.793	0.738992	12	0.703495	0.001222	0.000514
Yelaigai Suite 2	147.5	WL60421	268.2	26.07	29.949	0.764789	12	0.701996	0.001821	0.000566
	147.5	WL60422	320.6	46.59	19.758	0.743191	11	0.701764	0.001201	0.000377
	147.5	WL60423	313.9	66.27	13.74	0.730789	9	0.701981	0.000835	0.000263
	147.5	WL60424	310.2	109.8	8.184	0.720752	11	0.703592	0.000498	0.000162
	147.5	WL60425	319.1	238.4	3.876	0.712366	11	0.704239	0.000236	0.000083
	147.5	WL60427	362.5	142	7.397	0.719032	8	0.703522	0.000450	0.000145
	147.5	LW97079	324.4	24.43	38.129	0.783107	5	0.703162	0.002318	0.000710
	147.5	LW97080	303	26.59	32.725	0.771914	8	0.703300	0.001990	0.000613
Longtoushan 1 Suite 1	226.2	WL60420	134.9	304.3	1.283	0.708239	13	0.704111	0.000155	0.000084
	226.2	LW97076	142	286.6	1.435	0.708712	7	0.704097	0.000174	0.000087
	226.2	LW97077	145.7	315.8	1.378	0.708486	9	0.704053	0.000167	0.000086
	226.2	LW97078	143.4	289.8	1.432	0.708659	13	0.704051	0.000173	0.000093
	226.2	VII07B	149.8	449.9	0.9636	0.707001	8	0.703901	0.000117	0.000062
Longtoushan 2 Suite 2	117.3	WL60428	290.2	56.01	15.033	0.732715	10	0.707654	0.001352	0.000844
	117.3	WL60429	160.4	51.86	8.964	0.720767	6	0.705823	0.000806	0.000503
	117.3	LW97019	162.6	59.73	7.890	0.720282	12	0.707129	0.000709	0.000450
	117.3	LW97020	165.5	52.96	9.057	0.721215	9	0.706116	0.000814	0.000511
Xiaochengzi Suite 1	110.5	WL53063	169.3	295	1.661	0.708859	6	0.706250	0.000079	0.000032
	110.5	WL53064	186.8	283.8	1.906	0.709330	8	0.706337	0.000090	0.000038
	110.5	WL53065	181.1	299.1	1.753	0.709278	6	0.706526	0.000083	0.000033
	110.5	WL53066	175	274.3	1.847	0.709229	9	0.706328	0.000087	0.000038
	110.5	WL53068	166.9	272.1	1.776	0.709092	9	0.706303	0.000084	0.000037
	110.5	WL53069	165.9	278.3	1.725	0.709204	7	0.706495	0.000082	0.000034
	110.5	LW97016	188.1	251.5	2.165	0.709770	11	0.706370	0.000103	0.000045
Proterozoic gneisses	120	DB-101	8.95	258.5	0.1003	0.706519	12	0.706348	0.000003	0.000012
	120	DB-102	223.6	193.8	3.343	0.716817	11	0.711116	0.000114	0.000011
	120	FL62404	30.93	201.5	0.4443	0.707644	10	0.706886	0.000015	0.000010
	120	FL62405	216.9	130.8	4.807	0.721883	10	0.713685	0.000164	0.000010
	120	FL62406	287.9	426.3	1.956	0.712439	8	0.709103	0.000067	0.000008
Late Jurassic basalts	150	S1718	106.4	665.3	0.4598	0.705010	12	0.704030	0.000020	0.000012
	150	S1805	11.27	324.1	0.1001	0.704179	11	0.703966	0.000004	0.000011
	150	S1815	14.15	374	0.1087	0.704241	9	0.704009	0.000005	0.000009
	150	S2406	137.9	507.5	0.7806	0.706626	11	0.704962	0.000033	0.000011
	150	S2501	64.37	799.6	0.2308	0.706510	11	0.706018	0.000010	0.000011
	150	S2001	43.34	926.3	0.1342	0.704133	9	0.703847	0.000006	0.000009

Δ represents the uncertainty.

[a] $(^{87}Sr/^{86}Sr)_t = (^{87}Sr/^{86}Sr) - (^{87}Rb/^{86}Sr) \times (e^{\lambda t} - 1)$, $\lambda = 1.42 \times 10^{-11}$.

[b] $\pm \Delta(^{87}Sr/^{86}Sr)_t = \{(^{87}Sr/^{86}Sr) - [(^{87}Rb/^{86}Sr) \pm \Delta(^{87}Rb/^{86}Sr)] \times [e^{\lambda(t \pm \Delta t)} - 1]\} - \{(^{87}Sr/^{86}Sr) - (^{87}Rb/^{86}Sr) \times (e^{\lambda t} - 1)\}$, $\Delta(^{87}Rb/^{86}Sr) = \pm 2\%$.

[c] $\pm \Delta(^{87}Sr/^{86}Sr)_t = \{[(^{87}Sr/^{86}Sr) \pm \Delta(^{87}Sr/^{86}Sr)] - (^{87}Rb/^{86}Sr) \times [e^{\lambda(t \pm \Delta t)} - 1]\} - \{(^{87}Sr/^{86}Sr) - (^{87}Rb/^{86}Sr) \times (e^{\lambda t} - 1)\}$.

Table 5
Sm–Nd isotopic data

Pluton/suite	Sample no.	t (Ma)	Sm (ppm)	Nd (ppm)	$^{147}Sm/^{144}Nd$	$^{143}Nd/^{144}Nd$	$\pm 2\sigma_m$	$(^{143}Nd/^{144}Nd)_t$	$\varepsilon_{Nd}(t)$[a]	$\pm \Delta(^{143}Nd/^{144}Nd)_t$[b]	$\pm \Delta\varepsilon_{Nd}(t)$[c]	$\pm \Delta(^{143}Nd/^{144}Nd)_t$[d]	$\pm \Delta\varepsilon_{Nd}(t)$[c]	$f_{Sm/Nd}$[e]	$T1_{DM}$(Ma)[f]	$(^{147}Sm/^{144}Nd)_S$[g]	$T2_{DM}$(Ma)[h]
Maanzi Suite 2	WL852651	148.7	8.67	29.12	0.180144	0.512880	12	0.512705	5.04	0.000012	0.23	0.000014	0.27	−0.08	1225	0.115677	518
	WL852652	148.7	9.35	44.90	0.125873	0.512777	11	0.512655	4.06	0.000012	0.22	0.000013	0.24	−0.36	648	0.115677	596
	WL852653	148.7	7.05	30.41	0.131758	0.512796	11	0.512668	4.32	0.000012	0.22	0.000013	0.24	−0.33	659	0.115677	576
	WL852654	148.7	4.88	24.82	0.120573	0.512843	2	0.512726	5.45	0.000012	0.22	0.000004	0.06	−0.39	503	0.115677	486
	WL852655	148.7	7.33	36.68	0.120828	0.512793	9	0.512675	4.47	0.000012	0.22	0.000011	0.20	−0.39	587	0.115677	564
	WL852656	148.7	3.81	16.86	0.136746	0.512797	8	0.512664	4.24	0.000012	0.22	0.000010	0.18	−0.30	700	0.115677	582
	LW97064	148.7	7.91	40.87	0.119748	0.512812	13	0.512695	4.86	0.000012	0.22	0.000015	0.28	−0.39	549	0.115677	532
	LW97064-1	148.7	5.68	27.65	0.124197	0.512779	12	0.512658	4.13	0.000012	0.22	0.000014	0.26	−0.37	633	0.115677	591
	LW97065	148.7	5.45	28.49	0.115677	0.512769	11	0.512656	4.09	0.000011	0.22	0.000013	0.24	−0.41	593	0.115677	593
	LW97066	148.7	5.09	25.76	0.119408	0.512787	9	0.512671	4.38	0.000012	0.22	0.000011	0.20	−0.39	588	0.115677	571
Yelaigai Suite 2	WL60422	147.5	12.70	53.39	0.119093	0.512666	9	0.512551	2.01	0.000011	0.21	0.000010	0.20	−0.39	780	0.119093	780
	WL60424	147.5	6.45	32.25	0.120942	0.512620	7	0.512503	1.08	0.000011	0.21	0.000008	0.16	−0.39	871	0.119093	857
	WL60425	147.5	6.64	33.71	0.119168	0.512664	13	0.512549	1.97	0.000011	0.21	0.000014	0.27	−0.39	784	0.119093	784
	LW97079	147.5	10.58	41.01	0.143448	0.512665	11	0.512527	1.53	0.000011	0.22	0.000012	0.24	−0.27	1052	0.119093	820
	LW97080	147.5	11.96	45.33	0.268966	0.512690	8	0.512430	−0.35	0.000012	0.24	0.000010	0.20	0.37	−1278	0.119093	974
Longtoushan 2 Suite 2	LW97019	117.3	7.42	39.86	0.112574	0.512606	11	0.512520	0.64	0.000011	0.21	0.000014	0.27	−0.43	820	0.112574	820
	LW97020	117.3	7.50	40.28	0.134821	0.512626	6	0.512523	0.69	0.000011	0.22	0.000009	0.18	−0.31	1012	0.112574	816
Longtoushan 1 Suite 1	WL60420	226.2	3.33	17.07	0.117892	0.512753	12	0.512578	4.52	0.000018	0.36	0.000015	0.30	−0.40	632	0.117892	632
	LW97076	226.2	3.06	16.68	0.111006	0.512798	7	0.512634	5.60	0.000018	0.35	0.000010	0.20	−0.44	523	0.117892	545
	LW97077	226.2	3.55	18.90	0.113745	0.512747	12	0.512579	4.52	0.000018	0.36	0.000015	0.30	−0.42	615	0.117892	632
	LW97078	226.2	3.23	17.39	0.112455	0.512712	8	0.512546	3.88	0.000018	0.35	0.000011	0.22	−0.43	660	0.117892	685
	VII07B	226.2	4.73	25.51	0.112179	0.512667	3	0.512501	3.01	0.000018	0.35	0.000006	0.12	−0.43	726	0.117892	755
Xiaochengzi Suite 1	WL53063	110.5	4.34	22.79	0.115285	0.512431	12	0.512348	−2.89	0.000008	0.18	0.000013	0.27	−0.41	1113	0.115285	1113
	WL53064	110.5	4.22	22.33	0.114178	0.512456	9	0.512373	−2.39	0.000008	0.18	0.000010	0.21	−0.42	1063	0.115285	1073
	WL53065	110.5	4.19	25.31	0.100070	0.512472	10	0.512400	−1.88	0.000008	0.18	0.000011	0.23	−0.49	910	0.115285	1033
	WL53066	110.5	3.78	21.92	0.104150	0.512473	9	0.512398	−1.91	0.000008	0.18	0.000010	0.21	−0.47	942	0.115285	1036
	WL53068	110.5	4.20	23.65	0.107501	0.512436	8	0.512358	−2.68	0.000008	0.18	0.000009	0.19	−0.45	1025	0.115285	1097
	WL53069	110.5	4.31	26.75	0.098055	0.512428	15	0.512357	−2.71	0.000008	0.18	0.000016	0.33	−0.50	952	0.115285	1098
	LW97016	110.5	3.39	18.60	0.110326	0.512428	9	0.512348	−2.88	0.000008	0.18	0.000010	0.21	−0.44	1064	0.115285	1112
Proterozoic gneisses	DB-101	120	1.64	8.12	0.122200	0.512130	8	0.512034	−8.77	0.000008	0.15	0.000008	0.16	−0.38	1695		
	DB-102	120	4.41	21.27	0.125500	0.512210	11	0.512111	−7.26	0.000008	0.15	0.000011	0.21	−0.36	1621		
	FL62404	120	1.08	5.53	0.118100	0.512135	12	0.512042	−8.61	0.000008	0.15	0.000012	0.23	−0.40	1615		
	FL62405	120	4.20	18.39	0.137900	0.512193	10	0.512085	−7.78	0.000008	0.15	0.000010	0.20	−0.30	1918		
	FL62406	120	1.21	7.20	0.101600	0.512264	11	0.512184	−5.84	0.000008	0.15	0.000011	0.21	−0.48	1204		
Late Jurassic basalts	S1718	150	3.98	19.57	0.123100	0.512751	13	0.512630	3.61	0.000010	0.20	0.000013	0.25	−0.37	672		
	S1805	150	1.17	3.37	0.210600	0.512958	13	0.512751	5.98	0.000010	0.20	0.000013	0.25	0.07	9189		
	S1815	150	1.26	3.78	0.201100	0.512911	12	0.512714	5.24	0.000010	0.20	0.000012	0.23	0.02	2873		
	S2406	150	7.07	36.33	0.117800	0.512558	11	0.512442	−0.05	0.000010	0.20	0.000011	0.21	−0.40	941		
	S2501	150	8.20	44.53	0.111400	0.512400	12	0.512291	−3.01	0.000010	0.20	0.000012	0.23	−0.43	1117		
	S2001	150	10.54	51.11	0.124800	0.512843	8	0.512721	5.38	0.000010	0.20	0.000008	0.16	−0.37	527		

Δ represents the uncertainty.

[a] $\varepsilon_{Nd}(t)$ values were calculated relative to CHUR with the present-day values of $^{143}Nd/^{144}Nd = 0.512638$ and $^{147}Sm/^{144}Nd = 0.1967$ (Jacobsen and Wasserburg, 1980).

[b] $\pm \Delta(^{143}Nd/^{144}Nd)_t = \{(^{143}Nd/^{144}Nd) - [(^{147}Sm/^{144}Nd) \pm \Delta(^{147}Sm/^{144}Nd)] \times [e^{\lambda(t \pm \Delta t)} - 1]\} - \{(^{143}Nd/^{144}Nd) - (^{147}Sm/^{144}Nd) \times (e^{\lambda t} - 1)\}$, $\Delta(^{147}Sm/^{144}Nd) = \pm$ 1%.

[c] $\pm \Delta\varepsilon_{Nd}(t) = \pm \Delta(^{143}Nd/^{144}Nd)_t \times 10{,}000/(^{143}Nd/^{144}Nd)_t^{CHUR} = \pm \Delta(^{143}Nd/^{144}Nd)_t \times 10{,}000/(0.512638 - 0.1967 \times (e^{\lambda t} - 1))$.

[d] $\pm \Delta(^{143}Nd/^{144}Nd)_t = \{[(^{143}Nd/^{144}Nd) \pm \Delta(^{143}Nd/^{144}Nd)] - (^{147}Sm/^{144}Nd) \times [e^{\lambda(t \pm \Delta t)} - 1]\} - \{(^{143}Nd/^{144}Nd) - (^{147}Sm/^{144}Nd) \times (e^{\lambda t} - 1)\}$.

[e] $f_{Sm/Nd} = [(Sm/Nd)_{Sample}/(Sm/Nd)_{CHUR}] - 1 = [(^{147}Sm/^{144}Nd)_{Sample}/(^{147}Sm/^{144}Nd)_{CHUR}] - 1$.

[f] $T1_{DM} = 1/\lambda_{Sm} \times \ln\{1 + [(^{143}Nd/^{144}Nd)_{Sample} - (^{143}Nd/^{144}Nd)_{DM}]/[(^{147}Sm/^{144}Nd)_{Sample} - (^{147}Sm/^{144}Nd)_{DM}]\}$, where $(^{143}Nd/^{144}Nd)_{DM} = 0.51315$, $(^{147}Sm/^{144}Nd)_{DM} = 0.2137$ (Peucat et al., 1988), $\lambda_{Sm} = 6.54 \times 10^{-12}$ a^{-1}. DM: depleted mantle.

[g] $(^{147}Sm/^{144}Nd)_S$ refers to the value of the source rock that is represented by the highest or the lowest value from each pluton of Suite 1 or 2.

[h] $T2_{DM} = 1/\lambda_{Sm} \times \ln\{1 + [(^{143}Nd/^{144}Nd)_{Sample} - (\exp(\lambda_{Sm}t) - 1)[(^{147}Sm/^{144}Nd)_{Sample} - (^{147}Sm/^{144}Nd)_S] - (^{143}Nd/^{144}Nd)_{DM}]/[(^{147}Sm/^{144}Nd)_S - (^{147}Sm/^{144}Nd)_{DM}]\}$.

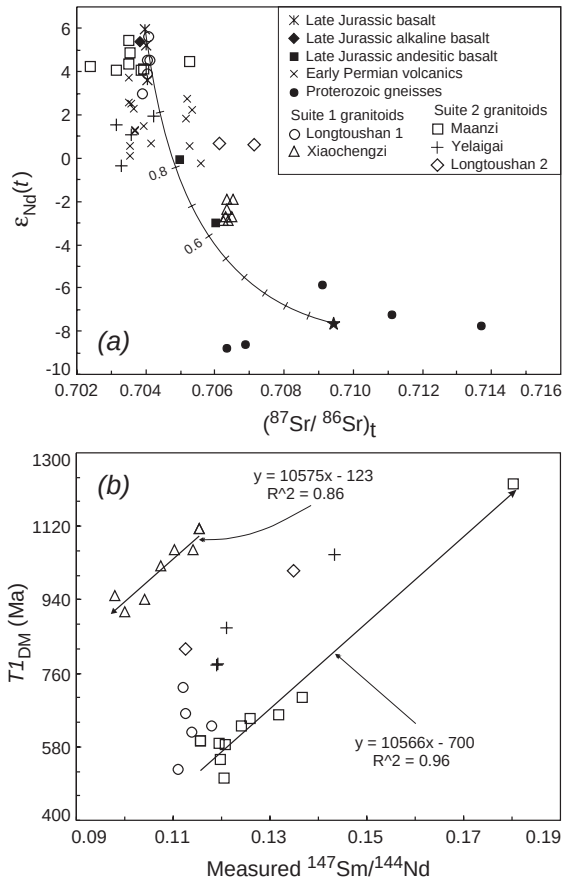

Fig. 13. (a) $\varepsilon_{Nd}(t)$ vs. $(^{87}Sr/^{86}Sr)_t$ plot of granitoids, the Late Jurassic basalts, and the Proterozoic gneisses in the Linxi area. The data of the Early Permian basalt (9 samples), trachyandesite (5), and basaltic andesite (1) are from Zhu, Y.F. (unpublished). Also shown is the hyperbola of simple mixing between underplated basalt, as represented by sample S1805, and the lower-crustal rock, as represented by the average compositions (the solid star) of the five Proterozoic gneiss samples (242.2 ppm Sr, 12.1 ppm Nd, 0.709428 $(^{87}Sr/^{86}Sr)_t$, −7.65 $\varepsilon_{Nd}(t)$). Tick marks on the mixing hyperbola represent the increment of 0.1 mass fraction basalt. (b) Measured $^{147}Sm/^{144}Nd$ vs. $T1_{DM}$ plot for the Linxi granitoids showing the overall positive correlation. Data of LW97080 from the Yelaigai that has a negative $T1_{DM}$ age is not shown. The arrow of the fitted correlation line points to the direction of Sm/Nd fractionation.

the melting depth was decreased to allow greater amounts of the old lower-crustal rock to be melted. Frost and Frost (1997) suggested that re-melting of underplated tholeiites by continued underplating produces the reduced rapakivi-type granites, among A-type granites. Kerr and Fryer (1993) and Poitrasson et al. (1995) proposed similar petrogenesis for A-type granites through interaction of mantle-derived magmas with the lower-crustal rock.

8.2. Fractional crystallization with or without the overprint of hydrothermal fluids as the cause of the geochemical variation of the Linxi granitoids

Several processes could be responsible for the geochemical variation of the two suites. These include crystal accumulation, fractional crystallization, magma mixing, crustal contamination, and overprint of hydrothermal fluids. Significant magma mixing and crustal contamination are not favored (see the previous

subsection). The Linxi granitoids show characteristic subhedral instead of cumulate textures. The analyzed samples lack positive Eu anomalies that would be present if these samples were cumulate considering that plagioclase is one of the major liquidus phases. Moreover, a cumulate–melt relationship between Suites 1 and 2 is untenable because their emplacement ages are different. Therefore, crystal accumulation is infeasible for the Linxi granitoids. In the following, mass-balance calculations were applied to each pluton or suite to determine if the geochemical variation could be ascribed to fractional crystallization with or without the overprint of hydrothermal fluids.

8.2.1. Major element modeling

We chose samples VII07B and WL53063 to represent the parent magmas for the Longtoushan 1 and the Xiaochengzi plutons, respectively, and WL60425 from the Yelaigai pluton for Suite 2. These samples show the lowest SiO_2 contents and the highest Sr, Eu, and Ba abundances within each pluton, and, hence, represent the least-fractionated granitoids. Because the data of Suite 2 are clustered together or form an integral trend (Fig. 8), they were modeled as a single set. To quantify the fractionation process, we used the equation

$$c_0^m - c_s^m \times (1-f) = c_1^m \times f$$

where c_0^m, c_s^m, and c_1^m refer to the content of major element oxide m in the parent magma, the crystallizing assemblage, and the residual melt, respectively; f to the mass fraction of the residual melt. Content c_s^m is calculated using the equation

$$c_s^m = \Sigma \alpha_{n/s} \times c_n^m$$

where c_n^m refers to the content of major element oxide m in mineral n; $\alpha_{n/s}$ to the mass proportion of mineral n in the crystallizing assemblage. Content c_n^m was evaluated by the molecular formula of mineral n, and the analysis of mineral chemistry using electron microprobe.

If c_n^m does not vary much during the fractional crystallization (c_0^m is a constant), c_1^m varies with $\alpha_{n/s}$ and f, so as to depict a fractionation trajectory. We tried to fit the fractionation trajectory to the variation trend in Fig. 8 by changing the value of $\alpha_{n/s}$. When the variation trend of all the major element oxides is approached, a reasonable estimation of value $\alpha_{n/s}$ is given. Moreover, when most of the data within a variation trend, especially for the most evolved granitoids, are approached by the fractionation trajectory, a reasonable estimation on the value of f is given.

Calculations for Suite 1 reveal that only a moderate degree of fractionation, ~ 12% for the Longtoushan 1 pluton and ~ 10% for the Xiaochengzi pluton, is necessary to generate the restricted compositional range. Fractionation phases include dominant hornblende, subordinate plagioclase and K-feldspar, minor biotite, ilmenite, and apatite. Calculations for Suite 2 were divided into two steps as required by the chemical variation. Calculation of Step 1 fractional crystallization accommodates the chemical gap between WL60425 and the remaining samples of Suite 2, whereas calculation of Step 2 fractionation models the variation trends of Suite 2. Step 2 fractionation (f=1–0.68) is characterized by removal of dominant plagioclase and K-feldspar, subordinate quartz and biotite, and trace apatite and ilmenite, without hornblende. However, fractionation of Step 1 (f=1–0.84) is characterized by removal of plagioclase, K-feldspar, quartz, biotite, hornblende, ilmenite, and apatite in decreasing order of proportion. Details of the calculation are summarized in Table 6. The fractionation trajectories were modeled to the three data sets (Fig. 8). In Figs. 8(b) and (e), the scattered data of Suite 2 cannot be adequately modeled. Enrichment by the hydrothermal fluid would be responsible for the K_2O scatter (Poitrasson and Pin, 1998), whereas the presence of some minor ferromagnesian minerals or iron oxides in the crystallizing assemblage makes the variation of MgO+FeO complicated.

Table 6
Trace element and rare earth element modelling

Mineral	Plagioclase	K-feldspar	Hornblende	Biotite	Apatite	Ilmenite	Quartz	Zircon	Allanite	Bulk D	Bulk D	Bulk D	Bulk D
Ref.[a]	1	2	3	4	5	1	1	6	7	Longtoushan 1	Xiaochengzi	Suite 2, Step 1	Suite 2, Step 2
Partition coefficients used													
Rb	0.105	1.75	0.014	3.2			0.041			0.366	0.532	0.792	0.885
Sr	15.633	5.4	0.022	0.447						4.32	2.41	5.67	5.68
Ba	1.515	11.45	0.044	23.533			0.022			2.64	3.76	4.69	5.90
Y	0.13		6	1.233	40	1.467		100	8.9	5.30	5.90	1.00	0.286
Nb	0.06	0.01	4	6.367	0.1	2.5		47.5	1.08	5.24	6.39	0.981	0.667
La	0.38	0.072	0.85	0.33	23.85	1.223	0.015	16.9	820	4.59	0.85	1.51	0.294
Ce	0.267	0.046	0.899	0.32	34.7	1.64	0.014	16.75	635	4.03	0.94	1.30	0.263
Nd	0.203	0.038	2.89	0.29	57.1	2.267	0.016	13.3	463	4.78	2.37	1.38	0.287
Sm	0.165	0.025	3.99	0.26	62.8	2.833	0.014	14.4	205	4.45	3.12	1.16	0.277
Eu	5.417	2.6	3.44	0.24	30.4	1.013	0.056	16	81	4.57	3.43	3.22	3.26
Gd	0.125	0.015	5.48	0.28	56.3	3	0.015	12	130	4.81	4.08	1.13	0.241
Tb	0.08	0.033	6	0.28	53.5	3.267	0.017	37	71	5.08	4.57	1.08	0.219
Dy	0.112	0.052	6.2	0.29	50.7	2.633	0.015	101.5	35.5	5.73	5.17	1.06	0.231
Yb	0.09	0.015	4.89	0.44	23.9	1.467	0.017	527	8.9	9.27	6.47	0.846	0.155
Lu	0.092	0.031	4.53	0.33	20.2	1.203	0.014	641.5	7.7	10.3	7.39	0.815	0.139
Mass fraction used										Range of residual melt fractions			
Suite 1													
Longtoushan 1	0.2293	0.1310	0.5487	0.0328	0.018	0.0246	0	0.0115	0.0041	1–0.88			
Xiaochengzi	0.1036	0.1362	0.6522	0.0856	0.0063	0	0	0.0161	0	1–0.90			
Suite 2, Step 1	0.4053	0.2603	0.0853	0.0896	0.0068	0.0102	0.1408	0.0003	0.00128	1–0.84			
Suite 2, Step 2	0.4396	0.293	0	0.0996	0.0026	0.0011	0.1641	0	9.00e−06	1–0.68			

Mass fractions are as fractions of the total removed mineralogy.

[a] References: (1) Nash and Crecraft, 1985; (2) Rb–Nb: Nash and Crecraft, 1985; REE: Mahood and Hildreth, 1983; (3) Arth, 1976; (4) Rb–Nb: Nash and Crecraft, 1985; REE: Arth, 1976; (5) Rb–Ba and REE: Arth, 1976; Y and Nb: Pearce and Norry, 1979; (6) Mahood and Hildreth, 1983; (7) Brooks et al., 1981.

8.2.2. Trace element and REE modeling

Variation in the concentrations of selected trace elements Rb, Sr, Ba, Y, Nb, and REE was modeled using the equation of Rayleigh fractional crystallization:

$$c_1^i = c_0^i \times f^{(D^i-1)}$$

where c_0^i and c_1^i refer to the concentration of element i in the parent magma and the residual melt, respectively, f to the mass fraction of the residual melt and D^i to the bulk distribution coefficient of i. Values of D^i were calculated using the equation

$$D^i = \Sigma \alpha_{j/s} \times D_j^i$$

where D_j^i refers to the partition coefficient of element i between mineral j and the residual melt; $\alpha_{j/s}$ to the mass proportion of mineral j in the crystallizing assemblage.

Trace element abundances of VII07B, WL53063, and WL60425 were used as c_0^i for the Longtoushan 1, the Xiaochengzi, and Suite 2, respectively. Values of f and $\alpha_{j/s}$ were obtained by major element modeling. The D_j^i values for dacite and rhyolite (Table 6) were used to calculate D^i. Because trace elements, especially REE, have strong affinities to accessory minerals, zircon and allanite were added to the crystallizing assemblage (Table 6). The fractionation trajectories were modeled to the three data sets (Figs. 9, 10 and 14).

As shown in Fig. 9, the decrease in concentrations of Sr, Ba, and Eu with increasing SiO_2 for both suites is accounted for by removal of feldspars from the remaining melt. The presence or absence of a significant amount of hornblende in the crystallizing assemblage for Suite 1 or 2 explains the decreasing or increasing Sm+Gd, Nb, Y, and Yb with decreasing Eu, respectively. In addition, the proportion of zircon in the crystallizing assemblage for Suites 1 and 2 (Steps 1 and 2) at 10^{-2} and 10^{-4} to 0 magnitudes, respectively, also contributes to the two contrasting trends. As shown in Fig. 10, the relative importance of hornblende over feldspars, coupled with the presence of a larger proportion of zircon, in the crystallizing assemblage for Suite 1 results in remarkable increases in La/Yb_N and Sr/Y ratios in the analyzed samples. On the other hand, the dominance of plagioclase and K-feldspar, integrated with the impoverishment or absence of zircon, in the crystallizing assemblage for Suite 2 causes the exceedingly low Sr/Y in the analyzed samples. Fractional crystallization also accounts for the constancy or slight increase and sharp increase in Ca/Sr, Rb/Sr, K/Ba, Ga/Al, and Rb/Ba with increasing SiO_2 for Suites 1 and 2, respectively (Fig. 14). However, the fractionation trajectory cannot adequately model the scattered data of Suite 2 in Figs. 9, 10 and 14 with regard to Sm+Gd, Nb, Y, Yb, K, and Rb. Additional process is required. Taylor et al. (1981) suggested that, during the late stage evolution of peralkaline granites, the F^-- or CO_3^{2-}-bearing magmatic fluid concentrates HREE, Y, Nb, and Rb among other elements. The presence of fluorite, and occurrence of dykes and pouch of pegmatite and aplite within and around Suite 2 granitoid plutons indicate the presence of F^--rich magmatic fluids during the evolution of Suite 2 granitoids. Overprint of these magmatic fluids would cause additional enrichment but scattered distribution of K and Rb (Figs. 14(c) and (e)), HREE, Nb, and Y (Figs. 9(d)–(g) and 10).

In conclusion, the consistent modeling using major and trace elements shows that fractional crystallization with or without the overprint of magmatic hydrothermal fluids is responsible for the chemical variations within Suites 2 and 1, and that specific crystallizing assemblages determine the variation trends of the two suites.

8.3. Nd isotope depleted mantle model age $T2_{DM}$ as calculated by a refined equation

As shown in Fig. 10, for Suite 1, LREE are enriched relative to HREE as indicated by increasing La/Yb_N, and (Sm+Gd) are depleted during fractional crystallization, hence resulting in decreasing Sm/Nd. For Suite 2, HREE

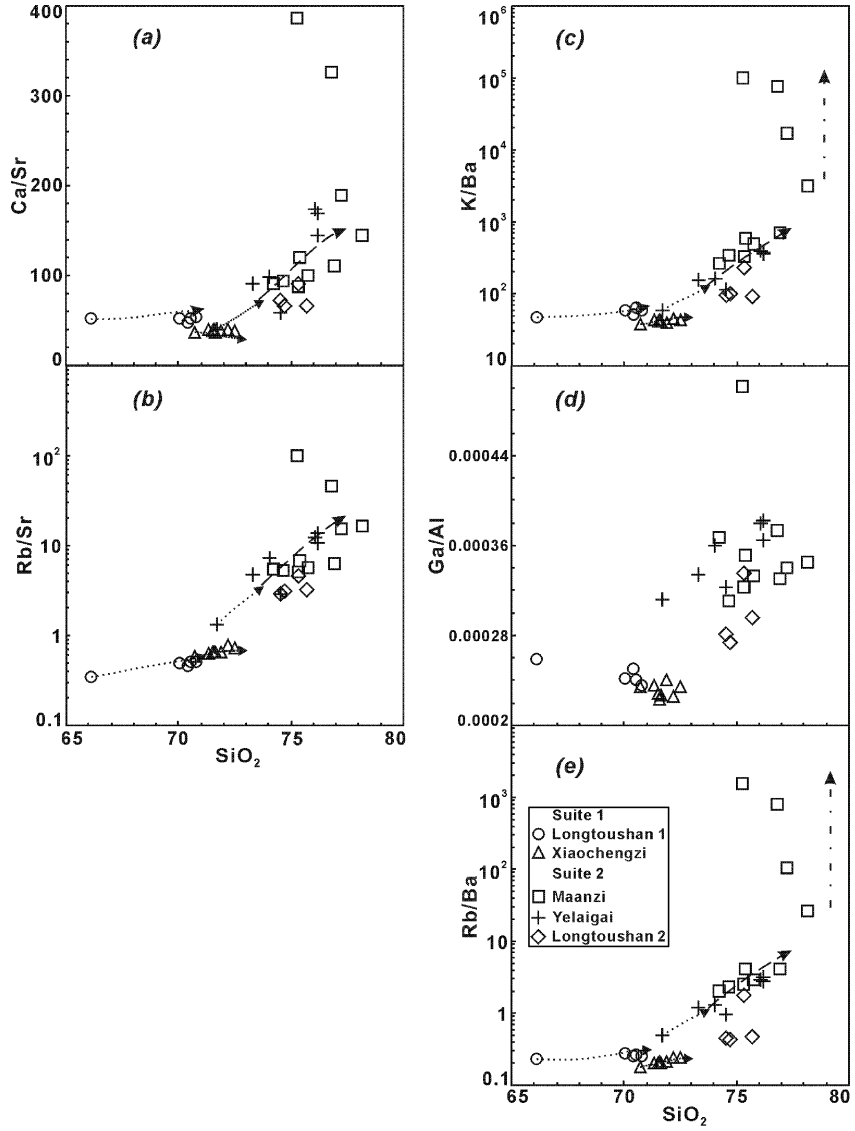

Fig. 14. SiO_2 vs. elemental ratio diagrams. The fractionation trajectory starting from the parent magma towards the residual melt (arrow-head) was modeled to the data sets of the Longtoushan 1 (dotted), the Xiaochengzi (dotted), and Suite 2 (dotted for Step 1, and dashed for Step 2). For details of the modeling, see Table 6. In (c) and (e), an arrowheaded dash-and-dotted line highlights the four data points from the Maanzi pluton that show extremely high K/Ba and Rb/Ba ratios.

tend to be enriched relative to LREE, and (Sm+Gd) are generally concentrated in the residual melt, resulting in increasing Sm/Nd. These modified Sm/Nd ratios cause inaccurate and diverse $T1_{DM}$ ages (Table 5). As shown in the $^{147}Sm/^{144}Nd$ vs. $T1_{DM}$ diagram (Fig. 13(b)), the Xiaochengzi and the Maanzi granitoids separately define positive correlation, whereas the Yelaigai and the Longtoushan 2 granitoids generally follow the two trends. So, $T1_{DM}$ ages depend strongly on the $^{147}Sm/^{144}Nd$ ratios. An increased or decreased Sm/Nd ratio would cause increased or decreased $T1_{DM}$ ages, respectively.

Instead of $T1_{DM}$, we propose a refined equation for calculating the depleted mantle model age, termed $T2_{DM}$. We have:

$$T2_{DM} = \frac{1}{\lambda}\ln\left[1 + \frac{(^{143}Nd/^{144}Nd)_S - (^{143}Nd/^{144}Nd)_{DM}}{(^{147}Sm/^{144}Nd)_S - (^{147}Sm/^{144}Nd)_{DM}}\right] \quad (1)$$

$$\left(^{143}Nd/^{144}Nd\right)_S = \left(^{143}Nd/^{144}Nd\right)_S^i + \left(^{147}Sm/^{144}Nd\right)_S\left(e^{\lambda t} - 1\right) \quad (2)$$

$$\left(^{143}Nd/^{144}Nd\right)_S^i = \left(^{143}Nd/^{144}Nd\right)_M^i = \left(^{143}Nd/^{144}Nd\right)_{sample} - \left(^{147}Sm/^{144}Nd\right)_{sample}\left(e^{\lambda t} - 1\right) \quad (3)$$

where the subscripts S, DM, and M refer to the source rock, the depleted mantle, and the magma, respectively; t the emplacement age of the granite pluton; and the isotopic ratios with or without superscript i the ratio at t or present-day.

By substituting Eqs. (3) into (2) and, then, substituting Eqs. (2) into (1), we obtain

$$T2_{DM} = \frac{1}{\lambda}\ln\left[1 + \frac{(^{143}Nd/^{144}Nd)_{sample} - \left(e^{\lambda t} - 1\right)\{(^{147}Sm/^{144}Nd)_{sample} - (^{147}Sm/^{144}Nd)_S\} - (^{143}Nd/^{144}Nd)_{DM}}{(^{147}Sm/^{144}Nd)_S - (^{147}Sm/^{144}Nd)_{DM}}\right]$$

The highest or the lowest $^{147}Sm/^{144}Nd$ value was chosen from each pluton of Suite 1 or 2 to represent the $(^{147}Sm/^{144}Nd)_S$ value, in order to offset Sm/Nd fractionation to a minimum. As shown in Table 5, the $T2_{DM}$ ages are less scattered than the $T1_{DM}$ ages within each pluton. $T2_{DM}$ ages for the Linxi granitoids, with the exception of the Xiaochengzi granitoids, are less than 1 Ga, again indicating a significant crustal growth during Phanerozoic times. $T2_{DM}$ ages of the Xiaochengzi pluton are around 1.1 Ga, providing another line of evidence that its source rock includes a significant amount of older lower-crustal material.

8.4. Petrogenesis of the Linxi granitoids

Petrography indicates that plagioclase is a liquidus phase in the least-fractionated rocks of both suites. Any prior crystal fractionation would have considerably increased Ca/Sr and Rb/Sr ratios. However, as shown in Fig. 14, the least-fractionated rocks of the Longtoushan 1, the Xiaochengzi, and Suite 2 have Ca/Sr ratios of 52.20, 37.07, and 39.74, Rb/Sr ratios of 0.35, 0.59, and 1.33, Rb/Ba ratios of 0.23, 0.18, and 0.5, and K/Ba ratios of 46.89, 37.21, and 59.89, respectively. These ratios are comparable to those of the parent magmas for the I- and A-type granites of the Chaelundi Complex, eastern Australia (Landenberger and Collins, 1996). These low ratios indicate little prior fractionation of plagioclase and K-feldspar. Therefore, we consider these rocks as parental magmas. As shown in Figs. 12(c) and (d), Suite 2 parent magma (WL60425) shows elevated concentrations of HFSE, LILE and LREE and moderate depletions of Ba, Sr, and Eu. These features have important implications for the petrogenesis of the Linxi granitoids.

We calculated the CIPW normative values for the parent magmas. By subtracting these values for the Longtoushan 1 pluton and Suite 2 from each other, we obtain

$$\text{Longtoushan 1} + 3.79\%\ Q + 5.96\%\ \text{Or} + 2.62\%\ \text{Ab} = \text{Suite 2} + 5.75\%\ \text{An} + 2.15\%\ \text{Di} + 2.23\%\ \text{Hy}$$

Differences between parent magmas of Suites 1 and 2 in the Or, Ab, An, Di, and Hy normative contents suggest a more abundant orthoclase component in Suite 2 parent magma, and more abundant An component

and ferromagnesian component in Suite 1 parent magma. This inference is supported by the petrography (Table 1).

In an extensional environment, I-type granites are produced by dehydration melting of the source involving a prior-underplated material (Landenberger and Collins, 1996) or by magma mixing (Cocherie et al., 1994). The voluminous Triassic I-type granitoids in the northern Inner Mongolia, as represented by the Longtoushan 1 pluton, are produced either by dehydration melting of dominantly underplated material or by magma mixing. Post-collisional thermal relaxation or rifting during the Triassic would provide the heat and material source. Suite 1 granitoids have abundant hornblende and biotite (Table 1), and are enriched in the LILE relative to HFSE with pronounced depletions of Nb and Ti (Fig. 11). These features imply a fluid-metasomatized mantle wedge as the ultimate source reservoir (Hawkesworth et al., 1991). Underplating during the Late Jurassic provides both continued heat supply and the newly mantle-derived material to the base of the lower crust. The heat supply is capable of elevating lower-crustal temperatures to above 850–900 °C (Clemens et al., 1986) or 900–950 °C (Huppert and Sparks, 1988). From the Late Jurassic to the Early Cretaceous times, melting of the underplated lower crust at elevated temperatures produced Suite 2 parental magma that shows an affinity to A-type granites. Geochemistry and petrography showing the preserved orthopyroxene, fluorite, and late crystallizing (interstitial) biotite (Table 1) both indicate the 'dry' nature for Suite 2 parental magma. However, crustal melting or magma mixing during the Triassic to yield the I-type granitoids did not result in dehydration or charnockitization of the protolith for Suite 2 that was dominantly underplated during the Late Jurassic. This fact casts doubt on the model of lower-crustal charnockitization as a prerequisite for generating A-type granites (Landenberger and Collins, 1996). In Suite 2 granitoids, FeO is much more enriched than MgO (Table 2), indicating a relatively low oxygen fugacity fO_2. The low fO_2 and low water activity α_{H_2O} of Suite 2 again indicate a derivation from the underplated tholeiite and its differentiated product (Frost and Frost, 1997) because the latter are dry and reduced. With decreasing α_{H_2O}, the melt would become enriched in normative orthoclase at the expense of plagioclase (Conrad et al., 1988; Ebadi and Johannes, 1991). This melting relation has resulted in more abundant K-feldspar and less abundant plagioclase, and, hence, moderate depletions of Sr, Ba, and Eu in Suite 2 parent magma. On the other hand, the low α_{H_2O}, and the resultant increase in α_{HF} led to the precipitation of fluorite (Frost and Touret, 1989), and brought about elevated concentrations of HFSE, LILE, and LREE in Suite 2 granitoids (Collins et al., 1982; Whalen et al., 1987).

Production of the I-type Xiaochengzi granitoids in the end of the Early Cretaceous postdates Suite 2. However, this pluton derives from a source region that has a larger proportion of the Proterozoic gneiss component probably at a higher level in the lower crust. In summary, the petrographic and geochemical properties of parent magmas for Suites 1 and 2 largely depend on the source rock composition.

8.5. Petrogenetic model

The petrogenetic sequence from Late Jurassic to Early Cretaceous volcanics and granitoids around the Linxi area can be interpreted in terms of progressive heating of the lower crust. When the basaltic magmatism is initiated in the early Late Jurassic, the crust is cold and, hence, brittle enough to allow some of the basalt to penetrate to the surface. A continued input of basaltic magma would add heat to the crust. The heating effect will be increased if most intrusions are focused at the base of the lower crust. Once extensive crustal melting is triggered, most of the basaltic magma will be trapped and become sills beneath the melting region. Basaltic volcanism marks the initiation of the Late Jurassic magmatism. Andesitic to trachytic volcanics are the product of extensive crustal melting or mixing of mantle- and crust-derived melts. Suite 2 granitoids and potassic rhyolites are melted from the underplated basalts with various amounts of the older crustal rock at elevated temperatures. With prolonged heating of the lower crust, melting occurs at decreasing depth to allow increasingly greater amounts of the older crustal rock to be melted.

9. Conclusions

Five granitoid plutons in the Linxi area, northern Inner Mongolia of China, were intruded from ~230 Ma to 111 Ma. These granitoids are divided into Suites 1 and 2 that correspond to I- and A-type granites, respectively. Source rock of the Linxi granitoids includes dominantly the mantle-derived material with various amounts of the Proterozoic gneiss in the lower crust. Although the Triassic I-type granitoids derive ultimately from the fluid-modified mantle, basaltic underplating provides the heat and material source for generating the Late Jurassic to Early Cretaceous granitoids. With the intrusion age of the Linxi granitoids becoming younger, increasingly greater amounts of the old crustal rock are involved in the melting. The I- and A-type granitoids in the Linxi area are genetically unrelated, whereas geochemical properties of their parent magmas essentially depend on the source rock. Fractional crystallization of hornblende and subordinate feldspars from the parent magma produced Suite 1 granitoids. However, fractional crystallization of plagioclase and alkali feldspar from the parent magma, with overprint of the magmatic hydrothermal fluid, produced Suite 2 granitoids.

Acknowledgements

We thank Dr. F. Poitrasson and Dr. R. Rudnick for providing valuable and constructive comments. Dr. F. Y. Wu is acknowledged for reviewing the early version of the manuscript. We thank Mr. R. Elmar for assistance in the zircon U–Pb isotope analysis. This research was supported by grant from the Innovation Program KZCX1-07-04 of the Chinese Academy of Sciences (CAS), grant 40472056 from the National Science Foundation of China, grant 2001CB409803 from the Ministry of Science and Technology of China, and the Studying Abroad Funds of the Education Bureau, CAS. **[TH]**

References

Arth, J.G., 1976. Behavior of trace elements during magmatic processes—a summary of theoretical models and their applications. J. Res. U.S. Geol. Surv. 4, 41–47.

Bacon, C.R., Macdonald, R., Smith, R.L., Baedecker, P.A., 1981. Pleistocene high-silica rhyolites of the Coso volcanic field, Inyo County, California. J. Geophys. Res. 86, 10223–10241.

Bowden, P., Kinnaird, J.A., Diehl, M., Pirajno, F., 1990. Anorogenic granite evolution in Namibia—a fluid contribution. Geol. J. 25, 381–390.

Brooks, C.K., Henderson, P., Ronsbo, J.G., 1981. Rare earth element partitioning between allanite and glass in the obsidian of Sandy Braes, northern Ireland. Mineral. Mag. 44, 157–160.

Bryant, C.J., Arculus, R.J., Chappell, B.W., 1997. Clarence River Supesuite: 250 Ma Cordilleran tonolitic I-type intrusions in eastern Australia. J. Petrol. 38, 975–1001.

Buck, W.R., 1991. Modes of continental lithospheric extension. J. Geophys. Res. 96, 20161–20178.

Chappell, B.W., 1999. Aluminium saturation in I- and S-type granites and the characterization of fractionated hapogranites. Lithos 46, 535–551.

Chen, Y., Chen, W., 1997. Mesozoic Volcanic Rocks: Chronology, Geochemistry, and Tectonic Background. Seismology Press, Beijing, pp. 279. in Chinese with English abstract.

Chen, F., Hegner, E., Todt, W., 2000. Zircon ages and Nd isotopic and chemical compositions of orthogneisses from the Black Forest, Germany: evidence for a Cambrian magmatic arc. Int. J. Earth Sci. 88, 791–802.

Clemens, J.D., Holloway, J.R., White, A.J.R., 1986. Origin of an A-type granite: experimental constraints. Am. Mineral. 71, 317–324.

Cocherie, A., Rossi, Ph., Fouillac, A.M., Vidal, Ph., 1994. Crust and mantle contributions to granite genesis—an example from the Variscan batholith of Corsica, France, studied by trace element and Nd–Sr–O-isotope systematics. Chem. Geol. 115, 173–211.

Coleman, D.S., Frost, T.P., Glazner, A.F., 1992. Evidence from the Lamarck granodiorite for rapid late Cretaceous crust formation in California. Science 258, 1924–1926.

Collins, W.J., Beams, S.D., White, A.J.R., Chappell, B.W., 1982. Nature and origin of A-type granites with particular reference to southeastern Australia. Contrib. Mineral. Petrol. 80, 189–200.

Conrad, W.K., Nicholls, I.A., Wall, V.J., 1988. Water-saturated and -undersaturated melting of metaluminous and peraluminous crustal compositions at 10 kb: evidence for the origin of silicic magmas in the Taupo Volcanic Zone, New Zealand, and other occurrences. J. Petrol. 29, 765–803.

Cui, Y., Russell, J.K., 1995. Nd–Sr–Pb isotopic systematics of the southern Coast Belt plutonic complex, southwestern British Columbia. Geol. Soc. Amer. Bull. 107, 127–138.

Davis, D.W., Krogh, T.E., 2000. Preferential dissolution of ^{234}U and radiogenic Pb from α-recoil-damaged lattice sites in zircon: implications for thermal histories and Pb isotopic fractionation in the near surface environment. Chem. Geol. 172, 41–58.

Davis, G.A., Darby, B.J., Zheng, Y., Spell, T.L., 2002. Geometric and temporal evolution of an extensional detachment fault, Hohhot metamorphic core complex, Inner Mongolia, China. Geology 30, 1003–1006.

DePaolo, D.J., 1981. Trace element and isotopic effects of combined wallrock assimilation and fractional crystallization. Earth Planet. Sci. Lett. 53, 189–202.

Ebadi, A., Johannes, W., 1991. Beginning of melting and composition of first melts in the system Qz–Ab–Or–H_2O–CO_2. Contrib. Mineral. Petrol. 106, 286–295.

Eberz, G.W., Nicholls, I.A., Mass, R., McCulloch, M.T., Whiteford, D.J., 1990. The Nd- and Sr-isotopic composition of I-type microgranitoid enclaves and their host rocks from the Swifts Creek pluton, southeast Australia. Chem. Geol. 85, 119–134.

Friedman, R.M., Mahoney, J.B., Cui, Y., 1995. Magmatic evolution of the southern coast Belt: constraints from Nd–Sr isotopic systematics and geochronology of the southern coast plutonic complex. Can. J. Earth Sci. 32, 1681–1698.

Frost, C.D., Frost, B.R., 1997. Reduced rapakivi-type granites: the tholeiite connection. Geology 25 (7), 647–650.

Frost, B.R., Touret, J.L.R., 1989. Magmatic CO_2 and saline melts from the Sybille monzosyenite, Laramie Anorthosite Complex, Wyoming. Contrib. Mineral. Petrol. 103, 178–186.

Frost, C.D., Frost, B.R., Chamberlain, K.R., Edwards, B.R., 1999. Petrogenesis of the 1.43 Ga Sherman batholith, SE Wyoming, USA: a reduced, rapakivi-type anorogenic granite. J. Petrol. 40 (12), 1771–1802.

Govindaraju, K., 1994. Compilation of working values and sample description for 383 geostandards. Geostand. Newsl. 18 (Special Issue), 1–158.

Graham, S.A., Hendrix, M.S., Johnson, C.L., Badamgarav, D., Badarch, G., Amory, J., Porte, M., Barsbold, R., Webb, L.E., Hacker, B.R., 2001. Sedimentary record and tectonic implications of Mesozoic rifting in southern Mongolia. Geol. Soc. Amer. Bull. 113, 1560–1579.

Han, B.-F., Wang, S.-G., Jahn, B.-M., Hong, D.-W., et al., 1997. Depleted-mantle source for the Ulungur River A-type granites from North Xinjiang, China: geochemistry and Nd–Sr isotopic evidence, and implications for Phanerozoic crustal growth. Chem. Geol. 138, 135–159.

Hawkesworth, C.J., Hergt, J.M., Ellam, R.M., McDermott, F., 1991. Element fluxes associated with subduction related magmatism. Philos. Trans. R. Soc. Lond. Ser. A 335, 393–405.

He, B.C., Tan, K.R., Wu, Q.H., 1994. Ages and Sr, Nd isotopic evidence of mantle source magmatite in the Bu's gold deposit, Jimunai County, northern Xinjiang. Geotecton. Metallogen. 18 (3), 219–228 (in Chinese with English abstract).

Hensel, H.-D., McCulloch, M.T., Chappell, B.W., 1985. The New England Batholith: constraints on its derivation from Nd and Sr isotopic studies of granitoids and country rocks. Geochim. Cosmochim. Acta 49, 369–384.

Hildreth, W., Halliday, A.N., Christiansen, R.L., 1991. Isotopic and chemical evidence concerning the genesis and contamination of basaltic and rhyolitic magma beneath the Yellowstone plateau volcanic field. J. Petrol. 32, 63–138.

Hoskin, P.W.O., Schaltegger, U., 2003. The composition of zircon and igneous and metamorphic petrogenesis. In: Hanchar, J.M., Hoskin, P.W.O. (Eds.), Zircon, Reviews in Mineralogy and Geochemistry, vol. 53, pp. 27–62.

Huppert, H., Sparks, R.S.J., 1988. The generation of granitic magmas by intrusion of basalt into continental crust. J. Petrol. 29, 599–624.

Jacobsen, S.B., Wasserburg, G.J., 1980. Sm–Nd isotopic evolution of chondrites. Earth Planet. Sci. Lett. 50, 139–155.

Keay, S., Collins, W.J., McCulloch, M.T., 1997. A three-component Sr–Nd isotopic mixing model for granitoid genesis Lachlan fold belt, eastern Australia. Geology 25, 307–310.

Kerr, A., Fryer, B.J., 1993. Nd isotope evidence for crust–mantle interaction in the generation of A-type granitoid suites in Labrador, Canada. Chem. Geol. 104, 39–60.

King, P.L., White, A.J.R., Chappell, B.W., Allen, C.M., 1997. Characterization and origin of aluminous A-type granites from the Lachlan Fold Belt, Southeastern Australia. J. Petrol. 38, 371–391.

Kinnaird, J., Bowden, P., 1987. African anorogenic alkaline magmatism and mineralization—a discussion with reference to the Niger–Nigerian province. Geol. J. 22, 297–340.

Kovalenko, V.I., Yarmolyuk, V.V., Kovach, V.P., Kotov, A.B., Kozakov, I.K., Sal'nikova, E.B., 1996. Sources of Phanerozoic granitoids in Central Asia: Sm–Nd isotope data. Geochem. Int. 34, 628–640.

Kravchinsky, V.A., Cogne, J.-P., Harbert, W.P., Kuzmin, M.I., 2002. Evolution of the Mongol–Okhotsk ocean as constrained by new paleomagnetic data from the Mongol–Okhotsk suture zone, Siberia. Geophys. J. Int. 148, 34–57.

Krogh, T.E., 1982. Improved accuracy of U–Pb zircon ages by the creation of more concordant systems using an air abrasion technique. Geochim. Cosmochim. Acta 46, 637–649.

Kwon, S.T., Tilton, G.R., Coleman, R.G., Feng, Y., 1989. Isotopic studies bearing on the tectonics of the west Junggar region, Xinjiang, China. Tectonics 8, 719–727.

Lamb, M.A., Badarch, G., 1997. Paleozoic sedimentary basins and volcanic arc systems of southern Mongolia: new stratigraphic and sedimentologic constraints. Int. Geol. Rev. 39, 542–576.

Landenberger, B., Collins, W.J., 1996. Derivation of A-type granites from a dehydrated Charnockitic lower crust: evidence from the Chaelundi Complex, Eastern Australia. J. Petrol. 37 (1), 145–170.

Liu, W., 1993. Whole rock isochron ages of plutons, crustal movements and evolution of tectonic setting in the Altay Mts., Xinjiang Uygur Autonomous Region. Geoscience of Xinjiang vol. 4. Geological Press, Beijing, pp. 35–50 in Chinese with English abstract.

Ludwig, K.R., 1988. Pbdat for MS-Dos—a computer program for IBM-PC compatibles for processing raw Pb–U–Th isotope data. Open-file Report 88-542, US Geol. Surv. 1–37.

Ludwig, K.R., 1994. Isoplot: a plotting and regression program for radiogenic-isotope data. A revision of the Open-File Rep, 91-445. US Geol. Surv. 1–45.

Mahood, G., Hildreth, W., 1983. Large partition coefficients for trace elements in high-silica rhyolites. Geochim. Cosmochim. Acta 47, 11–30.

Meng, Q.-R., 2003. What drove late Mesozoic extension of the northern China–Mongolia tract? Tectonophysics 369, 155–174.

Nakamura, N., 1974. Determination of REE, Ba, Fe, Mg, Na and K in carbonaceous and ordinary chondrites. Geochim. Cosmochim. Acta 38, 757–775.

Nash, W.P., Crecraft, H.R., 1985. Partition coefficients for trace elements in silicic magmas. Geochim. Cosmochim. Acta 49, 2309–2322.

Novak, S.W., Mahood, G.A., 1986. Rise and fall of a basalt–trachyte–rhyolite magma system at the Kane Springs Wash Caldera, Nevada. Contrib. Mineral. Petrol. 94, 352–373.

Parrish, R.R., 1987. An improved micro-capsule for zircon dissolution in U–Pb geochronology. Chem. Geol. 66, 99–102.

Pearce, J.A., Norry, M.J., 1979. Petrogenetic implications of Ti, Zr, Y and Nb variations in volcanic rocks. Contrib. Mineral. Petrol. 69, 33–47.

Peucat, J.J., Vidal, P., Bernard-Griffiths, J., Condie, K.C., 1988. Sr, Nd and Pb isotopic systematics in the Archaean low- to high-grade transition zone of southern India: syn-accretion vs. post-accretion granulites. J. Geol. 97, 537–550.

Pickett, D.A., Saleeby, J.B., 1999. Nd, Sr, and Pb isotopic characteristics of Cretaceous intrusive rocks from deep levels of Sierra Nevada batholith, Tehachapi Mountains, California. Contrib. Mineral. Petrol. 118, 198–215.

Poitrasson, F., Pin, C., 1998. Extreme Nd isotope homogeneity in a large rhyolitic province: the Estérel massif, southeast France. Bull. Volcanol. 60, 213–223.

Poitrasson, F., Duthou, J.L., Pin, C., 1995. The relationship between petrology and Nd isotopes as evidence for contrasting anorogenic granite genesis: examples of the Corsican province (SE France). J. Petrol. 36 (5), 1251–1274.

Poli, G.E., Tommasini, S., 1991. Model for the origin and significance of microgranular enclaves in calc-alkaline granitoids. J. Petrol. 32 (3), 657–666.

Poller, U., Liebetrau, V., Todt, W., 1997. U–Pb single-zircon dating under cathodoluminescence control (CLC-method): application to polymetamorphic orthogneisses. Chem. Geol. 139, 287–297.

Samson, S.D., McClelland, W.C., Patchett, P.J., Gehreless, G.E., Anderson, R.G., 1989. Evidence from neodymium isotopes for mantle contributions to Phanerozoic crustal genesis in the Canadian Cordillera. Nature 337, 705–709.

Sengör, A.M.C., Natal'in, B.A., 1996. Paleotectonics of Asia: fragments of a synthesis. In: Yin, A., Harrison, T.M. (Eds.), The Tectonic Evolution of Asia. Cambridge University Press. Cambridge, pp. 486–641.

Sengör, A.M.C., Natal'in, B.A., Burtman, V.S., 1993. Evolution of the Altaid tectonic collage and Paleozoic crustal growth in Eurasia. Nature 364, 299–307.

Taylor, S.R., McLennan, S.M., 1985. The Continental Crust: Its Composition and Evolution. Blackwell, Oxford.

Taylor, R.P., Strong, D.F., Fryer, B.J., 1981. Volatile control of contrasting trace element distributions in peralkaline granitic and volcanic rocks. Contrib. Mineral. Petrol. 77, 267–271.

Tepley F.J. III, Davidson, J.P., Tilling, R.I., Arth, J.G., 2000. Magma mixing, recharge and eruption histories recorded in plagioclase phenocrysts from El Chichón Volcano, Mexico. J. Petrol. 41 (9), 1397–1411.

Webb, L.E., Graham, S.A., Johnson, C.L., Badarch, G., Hendrix, M.S., 1999. Occurrence, age, and implications of the Yagan–Onch Hayrhan metamorphic core complex, southern Mongolia. Geology 27, 143–146.

Whalen, J.B., Currie, K.L., Chappell, B.W., 1987. A-type granites: geochemical characteristics, discrimination and petrogenesis. Contrib. Mineral. Petrol. 95, 407–419.

Whalen, J.B., Jenner, G.A., Longstaffe, F.J., Robert, F., Gariépy, C., 1996. Geochemical and isotopic (O, Nd, Pb and Sr) constraints on A-type granite petrogenesis based on the Topsails igneous suite, Newfoundland Appalachians. J. Petrol. 37 (6), 1463–1489.

Wood, D.A., Joron, J.L., Treuil, M., Norry, M., Tarney, J., 1979. Elemental and Sr isotope variations in basic lavas from Iceland and the surrounding ocean floor. Contrib. Mineral. Petrol. 70, 319–339.

Wu, F.Y., Jahn, B.M., Wilde, S., Sun, D.Y., 2000. Phanerozoic crustal growth: U–Pb and Sr–Nd isotopic evidence from the granites in northeastern China. Tectonophysics 328, 89–113.

Yarmolyuk, V.V., Kovalenko, V.I., 2001. The Mesozoic–Cenozoic of Mongolia. In: Dergunov III, A.B. (Ed.), Tectonics, Magmatism, and Metallogeny of Mongolia. Taylor & Francis Group, London, pp. 203–244.

Yin, A., Nie, S., 1996. A Phanerozoic palinspastic reconstruction of China and its neighboring regions. In: Yin, A., Harrison, T.M. (Eds.), The Tectonic Evolution of Asia. Cambridge University Press, Cambridge, pp. 442–485.

Zanvilevich, A.N., Litvinovsky, B.A., Wickham, S.M., Bea, F., 1995. Genesis of alkaline and peralkaline syenite–granite series: the Kharitonovo pluton (Transbaikalia Russia). J. Geol. 103, 127–145.

Zheng, Y., Wang, S.Z., Wang, Y., 1991. An enormous thrust nappe and extensional metamorphic core complex newly discovered in Sino-Mongolian boundary area. Sci. China 34, 1145–1152.

Zorin, Y.A., Belichenko, V.G., Yurutanov, E.Kh., Mazukabzov, A.M., Sklyarov, E.V., Mordvinova, V.V., 1995. The East Siberia transect. Int. Geol. Rev. 37, 154–175.